IOP Publishing
Plasma Sources Science and Technology
Plasma Sources Sci. Technol. **29** (2020) 074001 (19pp)
https://doi.org/10.1088/1361-6595/ab9156

Surface processes in low-pressure capacitive radio frequency discharges driven by tailored voltage waveforms

A Derzsi[1,2,5], B Horváth[2], Z Donkó[2] and J Schulze[1,3,4]

[1] Department of Physics, West Virginia University, Morgantown, WV 26506, United States of America
[2] Institute for Solid State Physics and Optics, Wigner Research Centre for Physics, 1121 Budapest, Hungary
[3] Institute of Electrical Engineering and Plasma Technology, Ruhr-University Bochum, 44780 Bochum, Germany
[4] Key Laboratory of Materials Modification by Laser, Ion and Electron Beams, School of Physics, Dalian University of Technology, People's Republic of China

E-mail: derzsi.aranka@wigner.hu

Received 27 January 2020, revised 8 April 2020
Accepted for publication 7 May 2020
Published 9 July 2020

Abstract

Particle-in-cell/Monte Carlo collisions (PIC/MCC) simulations are performed to investigate the sputtering and the secondary electron emission (SEE) in geometrically symmetric capacitively coupled Ar discharges with Cu electrodes driven by tailored voltage waveforms (TVWs). The driving voltage waveform is composed of multiple consecutive harmonics ($1 \leqslant N \leqslant 4$) of the fundamental frequency (13.56 MHz) and is tailored by adjusting the identical phases (θ) of the even harmonics. The simulations are based on a discharge model in which realistic approaches are implemented for the description of the SEE induced by electrons and heavy-particles at the electrodes, as well as for the sputtering of the electrodes by heavy-particles. In case of applying a single frequency, the voltage amplitude is varied ($250\ \mathrm{V} \leqslant \phi_1 \leqslant 2500\ \mathrm{V}$), while in case of applying multi-frequency TVWs, N and θ are varied at a fixed total voltage amplitude ($\phi_{\mathrm{tot}} = 1000$ V) at a low pressure of 0.5 Pa. By applying more than one harmonic to drive the discharge, the mean energy of Ar^+ ions and fast Ar atoms at the electrodes can be controlled by changing the phase angles. Due to the dependence of the sputtering yield on the heavy-particle energies, the flux of sputtered atoms can as well be controlled by the phase angles at both electrodes. The domain over which the sputtered atom flux can be varied is enlarged by adding more harmonics to the driving voltage waveform. For all conditions investigated, electron induced SEs (δ-electrons) induce strong ionization in the α-mode and dominate the ionization dynamics at high voltage amplitudes.

Keywords: plasma surface interaction, secondary electron emission, sputtering, voltage waveform tailoring, low pressure CCP

(Some figures may appear in colour only in the online journal)

1. Introduction

The control of particle properties at the electrodes of low-pressure capacitively coupled discharges is of key importance in the different plasma processing applications of surfaces [1–5]. Driving capacitively coupled plasmas (CCPs) by tailored voltage waveforms (TVWs) [6] offers better control of particle flux-energy distribution functions in technological plasmas compared to other discharge configurations, e.g. classical dual-frequency discharges [7–12]. TVWs can be generated as a sum of sinusoidal signals with a fundamental frequency and a number of its higher harmonics with defined phase shifts between them. The shape of the waveforms can

[5] Author to whom any correspondence should be addressed.

 © 2020 IOP Publishing Ltd Printed in the UK

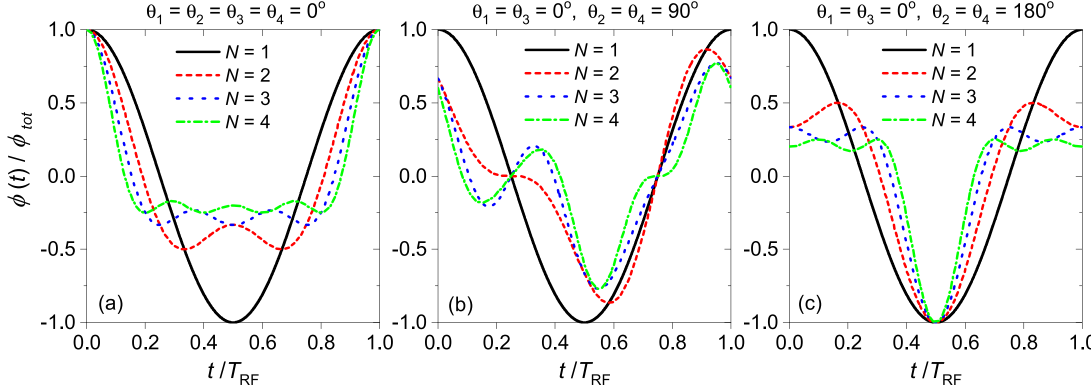

Figure 1. Normalized driving voltage waveforms, $\phi(t)/\phi_{\rm tot}$, for different numbers of consecutive harmonics, *N*, and different phase angles, θ_k. The time axis covers one period of the fundamental frequency, *f*, i.e. $T_{\rm RF} = 1/f$. 'Peaks'-type and 'valleys'-type waveforms are shown in panels (a) and (c), respectively [49].

be changed by varying the harmonics' amplitudes and phases. By changing the phase angles between the driving harmonics, the dc self-bias voltage caused by the asymmetric excitation waveform can be varied as well (Electrical Asymmetry Effect, EAE), which in turn allows the energy of ions to be controlled at the electrodes [13–23].

The Particle-in-cell method combined with Monte Carlo type treatment of the collision processes (PIC/MCC) [24–35] has been an important approach in the studies of a wide variety of phenomena in CCPs. The discharge models used in PIC/MCC simulations usually adopt several assumptions related to the description of the interaction of plasma species with the boundary surfaces. The reason for this is the lack of reliable surface coefficients for different combinations of the discharge gas and electrode material (with different surface properties) under various discharge conditions, required as input parameters in the simulations. However, the surface processes included in the discharge model and the assumptions made in the descriptions of these surface processes have a strong effect on the discharge characteristics obtained from PIC/MCC simulations of CCPs [36–49]. For instance, the value of the ion induced secondary electron emission coefficient (SEEC), γ, set as input parameter, was found to affect the discharge operation mode: at low values of the γ-coefficient (which was assumed not to depend on the discharge conditions and the surface properties) discharges operating in the α-mode were obtained (where ionization by electrons accelerated by the expanding sheaths dominates) [50–58], while at high values of the γ-coefficient the simulations resulted in discharges operating in the γ-mode (where ionization due to secondary electrons (SEs) in the sheaths is the dominant source of ionization) [50, 59–64]. Besides their influence on the plasma parameters the γ-coefficients used in the simulations were as well found to affect the quality of the control of ion properties at the electrodes in multi-frequency CCPs [49, 59, 60, 65–68].

Recently, the importance of the realistic description of the various surface processes in kinetic simulations of CCPs has attracted increasing attention. The simple models used to describe the secondary electron emission (SEE) induced by heavy-particles, which generally assume constant γ SE yield for these particles (independently of the discharge conditions and the surface properties) [50, 59–61, 64, 65, 69–72], have been replaced by more realistic approaches in some studies. Models which take into account the dependence of the SE yield due to heavy-particle impact on various factors, such as the energy of the incident particles, the electrode material and its surface conditions, have been implemented in PIC/MCC simulations of CCPs [36, 38–42, 47–49, 68]. In the simulation studies based on such models, so-called 'apparent' or 'effective' SEECs, γ^*, were determined self-consistently, which included the contributions of various plasma particles to the SEE based on their energy-dependent SE yields [73–75].

Realistic models for the description of the interaction of the electrons with the boundary surfaces have also been considered recently in PIC/MCC simulations of CCPs. Contrary to simple approaches (which typically take into account only the elastic electron reflection at a constant probability, e.g. 0.2 [76], independently of the discharge conditions and surface properties), the realistic models for the electron-surface interaction take into account the elastic reflection and the inelastic backscattering of electrons at the surfaces, as well as the emission of electron induced SEs (δ-electrons) upon primary electron impact [44, 45, 77, 78]. In general, the emission coefficients corresponding to these elementary processes are functions of the energy and the angle of incidence of the primary electrons hitting the surface and depend on the surface properties.

Previous simulation studies have shown that the realistic description of the SEE induced by both heavy-particles and electrons has a strong influence on the calculated discharge characteristics [36, 38–42, 44, 45, 47–49, 68, 77]. In these studies either the heavy-particle induced SEE or the electron induced SEE was described realistically. Simulation studies of CCPs in which realistic approaches for both heavy-particle induced SEE and electron induced SEE are combined can hardly be found [78]. Here, PIC/MCC simulations of geometrically symmetric capacitively coupled Ar discharges driven by TVWs are performed, based on a discharge model in which realistic approaches are implemented for the description of the SEE induced by both heavy-particles and electrons. Further, another surface process, the sputtering of the electrodes by energetic heavy-particles is also taken into account in a realistic manner [79–82]. While this process is generally

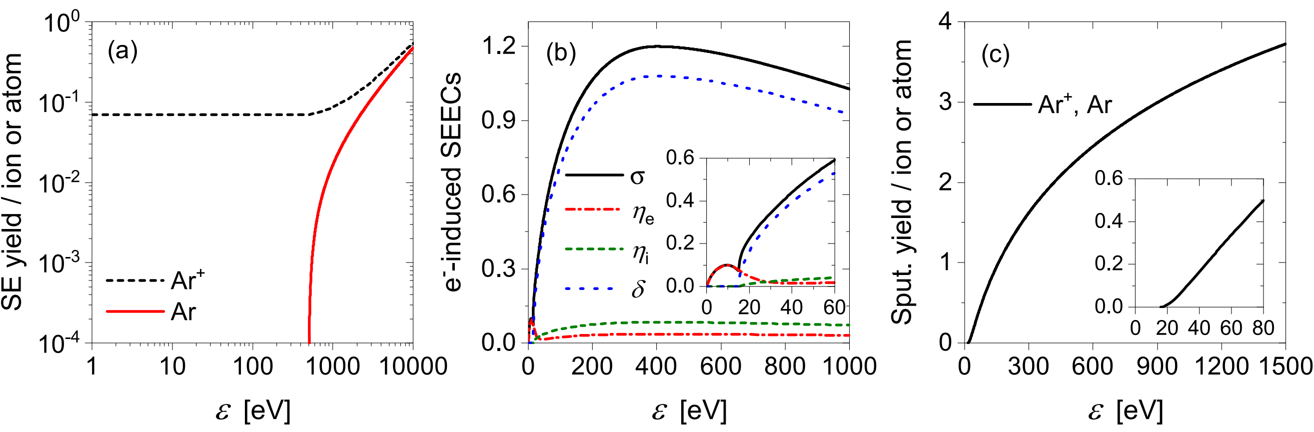

Figure 2. (a) SE yields on 'clean' metal surfaces, due to Ar^+ ions and Ar neutrals as a function of the incident particle energy, calculated according to [73]. (b) The total electron induced SEE coefficient (σ) and the partial emission coefficients of the elastic reflection (η_e), inelastic backscattering (η_i) and electron-induced SEE (δ) as a function of the incident electron energy, at normal incidence, for Cu surfaces. (c) The sputtering yield for Ar^+ ions and Ar atoms on Cu surfaces as a function of the energy of the particle, calculated according to [79]. The insets in panels (b) and (c) show the same quantities as the respective panels in the low-energy domain.

Table 1. Parameters of the realistic model of SEE for Cu surfaces.

#	Parameter	Description	Value	References
1	ε_0	The threshold energy for electron induced SEE	15 eV	[111]
2	$\varepsilon_{\max,0}$	The energy of PE at the maximum emission	400 eV	[111]
3	$\sigma_{\max,0}$	The maximum emission at normal incidence	1.2	[111]
4	k_s	Smoothness factor of the surface	1	[104]
5	$\varepsilon_{e,0}$	The threshold energy for elastic reflection	0 eV	[113]
6	$\varepsilon_{e,\max}$	The energy of PE at the maximum elastic reflection	10 eV	[112]
7	$\eta_{e,\max}$	The maximum of the elastic reflection	0.1	[112]
8	Δ_e	Control parameter for the decay of η_e	5 eV	[113]
9	r_e	Portion of elastically reflected electrons	0.03	[111]
10	r_i	Portion of inelastically reflected electrons	0.07	[111]

taken into account in discharge models describing direct current glow discharges [83–88], it is typically not included in PIC/MCC simulations of low-pressure CCPs. By including this process in the discharge model, the possibility to control the efficiency of sputtering at both electrodes via voltage waveform tailoring can be studied, which is highly relevant in plasma sputtering applications [89–96].

In the present simulations, the sputtering process and the role of SEs (focusing on electron induced SEs, i.e. δ-electrons) in the ionization dynamics is investigated. The driving voltage waveform is composed of $1 \leqslant N \leqslant 4$ consecutive harmonics of the fundamental frequency of $f = 13.56$ MHz, and is tailored by adjusting the identical phases of the even harmonics, θ. In all simulations, the gap length and the pressure is fixed at $L = 6.7$ cm and $p = 0.5$ Pa. Simulations are performed for single-frequency excitation of the discharge ($N = 1$) at different voltage amplitudes ($250\ \mathrm{V} \leqslant \phi_1 \leqslant 2500\ \mathrm{V}$), as well as for multi-frequency driving voltage waveforms ($1 \leqslant N \leqslant 4$) at a fixed total voltage amplitude ($\phi_{\mathrm{tot}} = 1000$ V). We assume that the electrodes are made of Cu, the parameters of the interaction of heavy-particles and electrons with the boundary surfaces are chosen accordingly. Cu is a material which is relevant for sputter applications and for which data for various surface processes are available in the literature. This work serves as proof-of-principle to study fundamental effects of realistic surface coefficients in PIC/MCC simulations of low-pressure CCPs. Further studies including other surface materials and gases need to be performed in the future.

The paper is structured in the following way: in section 2, the discharge model is outlined, including the description of the SEE induced by heavy particles and electrons, as well as the model for sputtering. The simulation results are presented in section 3. First, the results obtained for applying a single frequency waveform to drive the discharge are presented in section 3.1. Second, simulation results obtained by applying multiple frequency waveforms are presented and discussed in section 3.2. The conclusions are drawn in section 4.

2. Simulation method and discharge conditions

Our one-dimensional in space and three-dimensional in velocity space (1d3v) bounded plasma particle-in-cell code including a Monte Carlo treatment of the collision processes (PIC/MCC) is used to simulate argon discharges with electrodes made of copper [29, 30, 36]. We consider plane, parallel, and infinite electrodes, i.e. the studied discharges are geometrically symmetric. We assume that the surface conditions of both electrodes are identical. The background gas pressure is $p = 0.5$ Pa and a constant neutral gas temperature of 400 K

is assumed in the simulations. The background gas density is $n_{\mathrm{Ar}} \approx 9 \times 10^{19}$ m^{-3}. The electrode gap is $L = 6.7$ cm for all conditions investigated here. One of the electrodes is grounded, while the other one is driven by the following voltage waveform, composed of N harmonics of the fundamental frequency, $f = 13.56$ MHz:

$$\phi(t) = \sum_{k=1}^{N} \phi_k \cos(2\pi k f t + \theta_k), \tag{1}$$

where ϕ_k is the amplitude and θ_k is the phase angle of the kth individual harmonic ($k = 1, \ldots, N$). The amplitudes of the individual harmonics are set as $\phi_k = \phi_0(N - k + 1)/N$, where $\phi_0 = 2\phi_{\mathrm{tot}}/(N + 1)$ and $\phi_{\mathrm{tot}} = \sum_{k=1}^{N} \phi_k$. The phase angles provide a control over the electrical generation of the dc self-bias voltage [17]. By setting all phase angles to zero in equation (1), 'peaks'-type voltage waveforms are generated, while by setting the phase angles of the even harmonics to 180° in equation (1), 'valleys'-type waveforms are obtained. This is illustrated in figure 1, which shows the normalized driving voltage waveform, $\phi(t)/\phi_{\mathrm{tot}}$, for different numbers of consecutive harmonics, N, and different phase angles, θ_k. In this study, a maximum of four harmonics is applied ($1 \leqslant N \leqslant 4$) to drive the discharge, the value of the total voltage amplitude, ϕ_{tot}, is between 250 and 2500 V.

The particles included in the discharge model are electrons, Ar^+ ions, fast Ar neutrals (Ar^{f}), and sputtered Cu atoms. The following collision processes between these particles and the atoms of the background Ar gas are taken into account: for electrons, elastic scattering, excitation and ionization; for Ar^+ ions: elastic scattering (comprising an isotropic and a backward scattering channel), excitation and ionization; for Ar^{f} fast neutrals: isotropic elastic scattering, excitation and ionization; for Cu atoms: elastic scattering. The cross sections for these elementary collision processes are taken from [97–101].

The fast Ar atoms (Ar^{f}) are created in elastic collisions between Ar^+ ions and atoms of the background gas. These atoms can be 'born' with a wide range of superthermal energies. In our simulations, we, however, neglect the ones, which have an energy less than 23 eV, as these can neither cause excitation/ionization of Ar atoms, nor can induce SEE from the electrode surfaces and significant sputtering. The fast neutrals with an energy higher than 23 eV are traced until their energy falls below this threshold in further collisions or until they reach the electrodes. The Cu atoms are created by sputtering of the electrodes by energetic heavy particles (see below the description of the sputtering process). All sputtered Cu atoms (without any restriction on their kinetic energy) are traced in the discharge gap until they reach one of the electrodes. The depletion of the Ar neutral density due to sputtered Cu atoms is small under the conditions investigated here and, therefore, is neglected in the simulations (the density of Cu atoms is about three orders of magnitude lower than the density of the background Ar gas). Similarly to the neutral species, the Ar^+ ions are traced in the discharge gap until they arrive at the electrodes. Unlike heavy-particles, electrons are not always absorbed at the electrodes, they can be reflected from the electrode surfaces (see the model for the electron-surface interaction below).

We note that Cu^+ ions are not included in the present model. While these ions can have significant density under specific discharge conditions (at high pressures and high voltages) [84, 102], where sputtering by metal ions (i.e. self-sputtering) becomes also important [83, 94–96], this is not the case under the conditions investigated here.

In all simulations, the number of superparticles traced is around 10^5 for the different species (adjusted by using different superparticle weights for the different species). The computational grid is composed of 500–1700 points between the electrodes and the RF period (T_{RF}) is split into 5000–17 000 time steps.

2.1. Plasma-surface interactions

In the discharge model used in this study, the interactions of the different plasma species with the boundary surfaces are described precisely. Realistic models previously developed to describe specific plasma-surface interactions in PIC/MCC simulations of CCPs are combined here, as well as new surface processes included. Namely, the SEE induced by both heavy-particles and electrons is treated realistically and the sputtering of the electrodes by energetic heavy-particles is also taken into account.

2.1.1. Heavy-particle induced SEE

The SE yield due to bombardment of the electrode surfaces by fast neutrals and ions depends on the particle energy, as well as on the surface conditions. Measured SE yields for Ar ions and fast neutrals have been reported in [73] for different metal surfaces, and analytical formulas for the calculation of the SE yields due to these particles as functions of their energy have been provided for 'dirty' surfaces and 'clean' surface conditions. According to [73], 'clean' denotes atomically clean surface conditions (e.g. sputtered surfaces in ultra high vacuum environment), while 'dirty' refers to surfaces under typical laboratory conditions (treated by the standard chemical and mechanical cleaning procedures, gas-covered or oxidized samples). As we focus on discharges operated at low pressure and high voltages, we expect the sputtering of the electrodes to be significant, and, therefore, we assume that the electrode surfaces are atomically clean. The SE yields due to Ar^+ ions and Ar^{f} neutrals, γ_{i} and γ_{a}, respectively, are calculated as a function of their energy, ε, based on the formulas given in [73] for 'clean' metal surface conditions:

$$\gamma_{\mathrm{i}}(\varepsilon) = 0.07 + 1 \times 10^{-5}(\varepsilon - 500)^{1.2}/[1 + (\varepsilon/70000)^{0.7}], \tag{2}$$

$$\gamma_{\mathrm{a}}(\varepsilon) = 1 \times 10^{-5}(\varepsilon - 500)^{1.2}/[1 + (\varepsilon/70000)^{0.7}]. \tag{3}$$

γ_{i} and γ_{a} as a function of the particle energies are shown in figure 2(a). Based on the energy-dependent SE yields of the individual Ar^+ ions and Ar^{f} neutrals bombarding the electrodes, an effective SEEC, γ^*, can be determined self-consistently in the simulations at each electrode [74, 75]:

$$\gamma^* = \frac{\sum_{k=1}^{N_i} \gamma_i(\varepsilon_k) + \sum_{k=1}^{N_a} \gamma_a(\varepsilon_k)}{N_i}, \tag{4}$$

where N_i and N_a are the total number of Ar^+ ions and Ar^f atoms reaching a given electrode during an RF period. ε_k is the energy of the kth ion or atom at arrival at the electrode.

2.1.2. Electron induced SEE

The electron-surface interaction is described according to a realistic model presented in [44]. In this model, the total yield of SEs (σ) due to primary electrons bombarding the surface is composed of elastically reflected electrons, inelastically backscattered electrons and electron-induced SEs (δ-electrons or 'true' SEs):

$$\sigma = \eta_e + \eta_i + \delta, \tag{5}$$

where η_e is the elastic reflection yield, η_i is the inelastic backscattering yield, and δ is the electron-induced SE yield (yield of δ-electrons). The total SE yield and the partial emission coefficients are determined as proposed in [103–105], by taking into account the energy and angle of incidence of the primary electrons, as well as the surface properties. A detailed description of the model can be found in the work of Horváth *et al* [44]. The surface properties are taken into account via material specific input parameters, e.g. the maximum electron induced SEE at normal incidence, $\sigma_{max,0}$, and the primary electron energy at maximum SEE, $\varepsilon_{max,0}$. For most metal surfaces, $\sigma_{max,0}$ is less than 2 and can reach values higher than 10 for some oxides, while $\varepsilon_{max,0}$ is generally between 100 and 1000 eV [104–110]. Here, the parameters of the model are set for Cu surfaces. These parameters, listed in table 1, are the same as those used in a recent study by Liu *et al* [77].

The total electron-induced SEEC, σ, and the partial emission coefficients, η_e, η_i and δ, for Cu surfaces are shown in figure 2(b) as a function of the electron energy at normal incidence. At low electron energies σ increases rapidly, at a primary electron energy of $\varepsilon_{max,0} = 400$ eV reaches a maximum value of $\sigma_{max,0} = 1.2$, and decreases towards high electron energies. Compared to normal incidence, the SE yield is higher for oblique impact [104]. This effect is taken into account in the model. It is assumed that 7% of the emitted SEs are inelastically backscattered electrons (set by the r_i parameter), while at high particle energies 3% of the emitted SEs are elastically reflected electrons (set by the r_e parameter). At low primary electron energies the maximum of the elastic reflection yield is $\eta_{e,max} = 0.1$ at an electron energy of $\varepsilon_{e,max} = 10$ eV. The threshold energy for electron-induced SEE is $\varepsilon_0 = 15$ eV.

2.1.3. Sputtering

The Cu atoms are created by sputtering of the electrode material by energetic heavy particles. The sputtering yields for the different heavy particle species (Ar^+ and Ar^f) are calculated as a function of the energy of the incident particle, ε, according to the empirical formula of Matsunami *et al* [79]:

$$Y(\varepsilon) = 0.42 \frac{\alpha^* Q K s_n(\varepsilon_1)}{U_s(1 + 0.35 U_s s_e(\varepsilon_1))} [1 - (E_{th}/\varepsilon)^{1/2}]^{2.8}, \tag{6}$$

where α^*, Q and E_{th} are empirical parameters, U_s is the sublimation energy in eV, $s_n(\varepsilon_1)$ and $s_e(\varepsilon_1)$ are Lindhard's elastic and inelastic reduced stopping cross sections [101], ε_1 is the reduced energy, K is a conversion factor [79]. The energy dependence of the sputtering yield of Ar species on a Cu surface is shown in figure 2(c). The threshold energy for sputtering is 16 eV. The sputtering yield is higher than 1 for particle energies above ~160 eV and increases with increasing particle energies. The sputtered particle flux is determined by the flux and energy distribution of ions and fast neutrals impinging the surfaces and the corresponding sputtering yield. The energy distribution of the sputtered Cu atoms follows a Sigmund–Thompson distribution [114], while the emission angle of the sputtered atoms is sampled from a cosine distribution [115].

3. Results

First, the sputtering process and the role of δ-electrons in the ionization dynamics is analyzed in case of applying a single-frequency excitation ($N = 1$), in section 3.1. Subsequently, results obtained for multi-frequency ($N \geqslant 2$) driving voltage waveforms are discussed in section 3.2.

3.1. Single-frequency driving voltage waveforms

Figure 3 shows various discharge characteristics, such as the density of different heavy-particle species in the center of the discharge, their contribution to the sputtering of the electrode material, the mean heavy-particle energies and fluxes at the electrodes, as a function of the driving voltage amplitude, ϕ_1, for $N = 1$ (single-frequency excitation). By increasing ϕ_1, the density of Ar^+ ions and sputtered Cu atoms increases in the discharge center (figure 3(a)). While at $\phi_1 = 250$ V both species have a density of about 1.5×10^{15} m^{-3}, the density of Ar^+ ions increases by a factor of about 5 and the Cu atom density increases by a factor of about 30 by changing ϕ_1 to 2500 V. The density of Ar^f atoms is low in the discharge center (by about three orders of magnitude lower than the plasma density). Under the studied discharge conditions, most of the sputtering is caused by Ar^+ ions (figure 3(b)), their contribution to the total sputtering is between 79% and 91% (slightly decreases towards higher ϕ_1) for all voltage amplitudes, while that of Ar^f neutrals is between 9% and 21% (slightly increases towards higher ϕ_1). The importance of these plasma species in the sputtering process, as well as the steeply rising density of sputtered Cu atoms as a function of the driving voltage amplitude can be understood based on the flux-energy distributions of heavy particles at the electrodes.

For all the different heavy-particle species, a significant increase of the mean particle energies at the electrodes is found by increasing ϕ_1 from 250 to 2500 V (figure 3(c)). The lowest mean particle energies are obtained for Cu atoms (below 20 eV for all ϕ_1), while the highest mean particle energies are found in case of Ar^+ ions, which can be accelerated by the high electric field in the sheaths. The mean energy of Ar^+ ions at the electrodes is between 100 and 700 eV, while the mean energy of Ar^f neutrals changes from 60 to 300 eV by

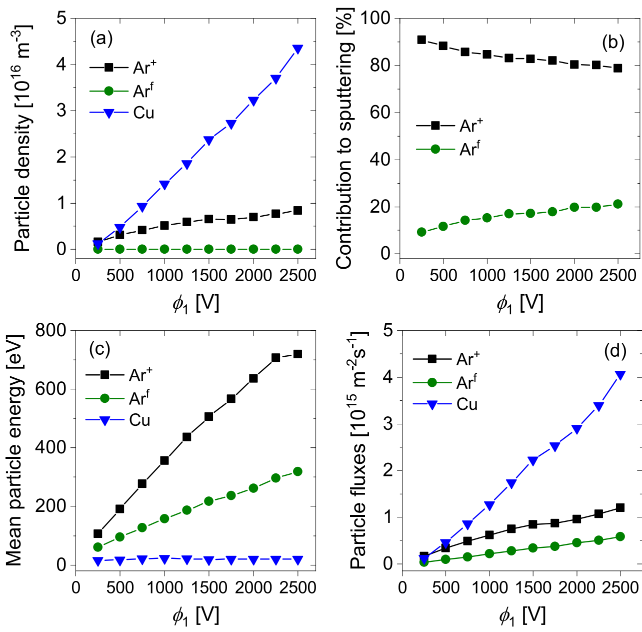

Figure 3. (a) The density of heavy particles (Ar^+, Ar^f, and Cu) in the center of the discharge, (b) their contribution to the sputtering of the Cu electrodes, (c) the mean energy and (d) incoming fluxes of heavy particles at the electrodes, as a function of the driving voltage amplitude, ϕ_1. Only atoms with energy above 23 eV are taken into account as Ar^f. Discharge conditions: $p = 0.5$ Pa, $L = 6.7$ cm, $f = 13.56$ MHz, $N = 1$.

increasing ϕ_1 from 250 to 2500 V. The flux-energy distributions of Ar^+ ions and Ar^f atoms bombarding the electrodes are shown in panels (a) and (b) of figure 4 for different values of the driving voltage amplitude. Under such conditions, significant sputtering of the electrodes is caused by Ar^+ and Ar^f particles. The sputtering yield for Ar particles is higher than 1 for particle energies above 160 eV and increases with increasing particle energies (figure 2(c)): at 300 eV the sputtering yield is 1.6 Cu atoms/Ar particle, while it reaches 2.6 at particle energies of 700 eV. The high sputtering yields by Ar^+ and Ar^f at high particle energies and the increasing flux of these particles to the electrodes by increasing ϕ_1 (as a result of the higher plasma density at higher driving voltage amplitudes) lead to the enhancement of the sputtering process and to the strong increase of the peak Cu density in the discharge as ϕ_1 is increased (figure 3(a)). By increasing ϕ_1, more Ar^f neutrals are created by energetic Ar^+ ions via elastic collisions in the sheaths. The flux of Ar^f atoms to the electrodes, as well as their contribution to the total sputtering increase, i.e. their importance in the sputtering process becomes more significant at high voltage amplitudes (figure 3(b)). Consequently, the contribution of Ar^+ to the sputtering slightly decreases by increasing ϕ_1 (figure 3(b)).

The increase of the Cu density by increasing ϕ_1 can also be observed in figure 5. This figure shows the time-averaged density distributions of various plasma species in the discharge gap for different values of ϕ_1. At all ϕ_1, Cu atoms are uniformly distributed within the gap due to the equal net sources for Cu atoms at both electrodes. Compared to the plasma density, the Cu density is higher by a factor of about 1.6 at $\phi_1 = 500$ V (5×10^{15} m^{-3} vs 3.1×10^{15} m^{-3}), while it is about 5 times higher at $\phi_1 = 2500$ V (4.2×10^{16} m^{-3} vs 8.3×10^{15} m^{-3}). However, the Cu density is at least three orders of magnitude lower than the background Ar gas density at 0.5 Pa ($n_{Ar} \approx 9 \times 10^{19}$ m^{-3}) at all ϕ_1. Therefore, the depletion of the Ar gas density due to Cu atoms is justified to be neglected. In the following, the effects of SEs on the discharge characteristics are analyzed, with focus on the role of electron induced SEs (δ-electrons) in the ionization dynamics. Their influence on the discharge characteristics has previously been investigated by using discharge models in which a constant heavy-particle induced SEEC, γ, was assumed, neglecting the dependence of the SE yields on the heavy-particle energies and on the surface conditions [44, 45, 77]. Here, the heavy-particle induced SEECs are calculated self-consistently in the simulations.

Figure 6 shows the self-consistently calculated effective SEEC, γ^*, as a function of the driving voltage amplitude, ϕ_1 taking values between 250 and 2500 V. The values of γ^* obtained from the simulations are low ($0.07 \leqslant \gamma^* < 0.0825$), compared to the values of the (constant) γ-coefficients typically assumed in PIC/MCC simulations of CCPs (e.g. $\gamma = 0.1$ is often set; in some cases $0.1 < \gamma \leqslant 0.4$ is used, reflecting to some extent characteristics of the electrode material and/or the surface conditions). For voltage amplitudes of $\phi_1 \leqslant 1250$ V, the effective γ^* is 0.07. At these voltage amplitudes only Ar^+ ions induce SEE at the electrodes. For $\phi_1 \leqslant 1250$ V the Ar^+ ion energies at the electrodes are below 500 eV (see figure 4(a)) and the SE yield due to Ar^+ impact is 0.07 for these particle energies (figure 2(a)). This corresponds to the potential emission by slow ions under clean surface conditions. At voltage amplitudes of $\phi_1 > 1250$ V, the SE yields due to Ar^+ ions with energies higher than 500 eV (figure 4(a)) are slightly higher than 0.07 (figure 2(a)), and Ar^f atoms can also generate SEs at the electrodes (see the flux-energy distribution of Ar^f atoms in figure 4(b)). The variation of the particle energies and their SE yields at the electrodes as a function of ϕ_1 leads to γ^* slightly increasing at high voltage amplitudes.

Figure 7 shows the spatio-temporal distributions of the total ionization rate (first row) and the electric field (second row) for different values of the driving voltage amplitude: $\phi_1 = 500$ V (first column), $\phi_1 = 1500$ V (second column), and $\phi_1 = 2500$ V (third column). At $\phi_1 = 500$ V, the discharge operates in the α-mode, i.e. the ionization is dominated by electrons that are accelerated at the expanding sheath edge. At the low pressure of 0.5 Pa, one beam of highly energetic electrons is generated at both electrodes during an RF period as the sheath expands, which causes ionization in the bulk region (figure 7(a)). Most of these beam electrons hit the collapsing sheath at the opposing electrode. At the electrodes, depending on their energy, they can be reflected or can induce emission of δ-electrons (figure 2(b)). At higher voltage amplitudes, the α-mode ionization is enhanced (figures 7(b) and (c)). At $\phi_1 = 1500$ V and $\phi_1 = 2500$ V, an electric field reversal at each electrode during sheath collapse can also be observed (figures 7(e) and (f)), with maximum values of about 35 and 120 Vcm^{-1}, respectively.

The spatio-temporal distribution of the ionization rate obtained here for high voltage amplitudes is different from that obtained in a previous simulation study of Horváth *et*

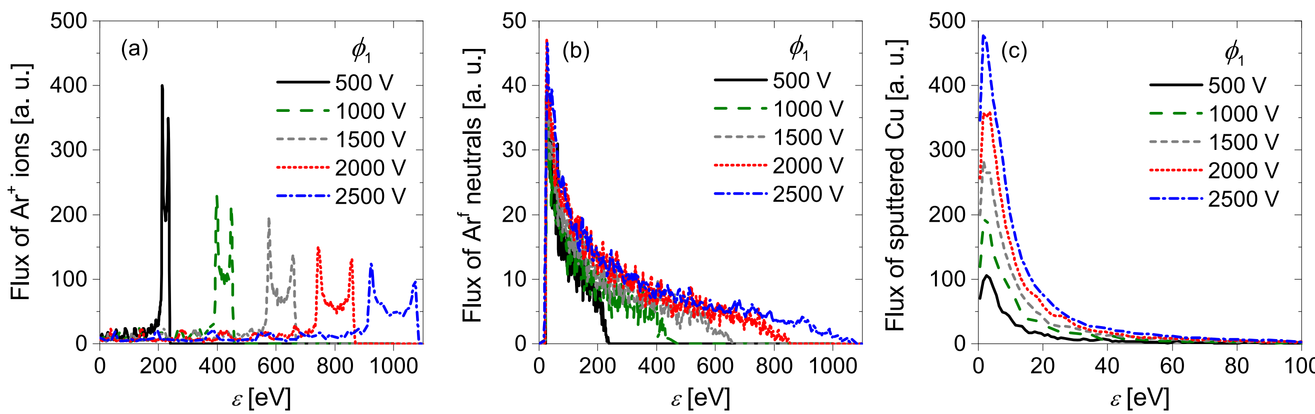

Figure 4. Flux-energy distribution of (a) Ar^+ ions and (b) Ar^f atoms bombarding the electrodes (incoming heavy-particle fluxes), and (c) flux-energy distribution of Cu atoms sputtered from the electrodes (outgoing Cu flux) as a function of the ion/atom energy, ε, for different values of the driving voltage amplitude, ϕ_1. The vertical scales are in arbitrary units and can be compared to each other. Discharge conditions: $p = 0.5$ Pa, $L = 6.7$ cm, $f = 13.56$ MHz, $N = 1$.

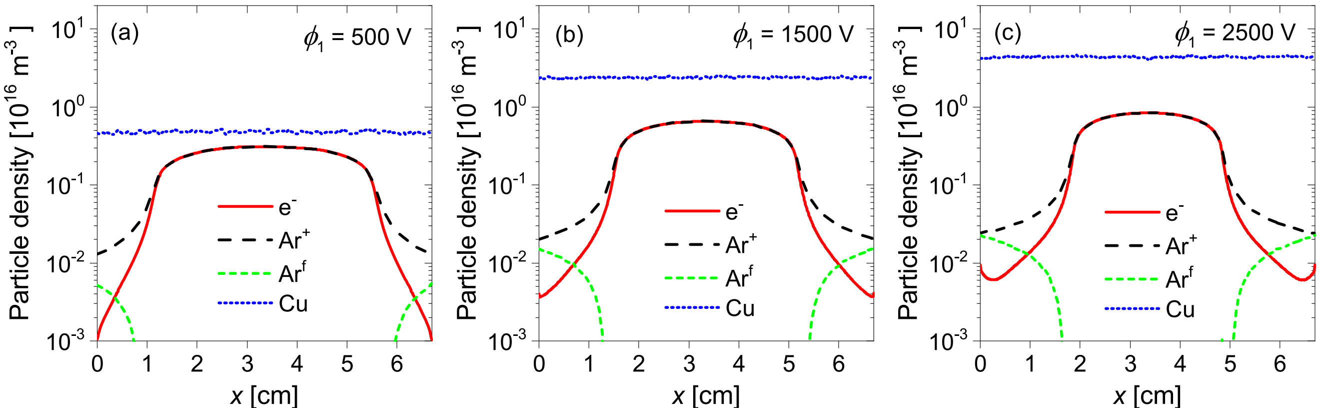

Figure 5. Time-averaged density distributions of heavy-particles and electrons in the discharge gap for different values of the driving voltage amplitude, ϕ_1: (a) $\phi_1 = 500$ V, (b) $\phi_1 = 1500$ V and (c) $\phi_1 = 2500$ V. Discharge conditions: $p = 0.5$ Pa, $L = 6.7$ cm, $N = 1$.

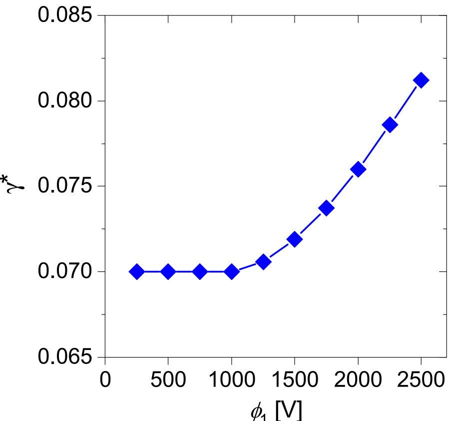

Figure 6. The self-consistently calculated SEEC, γ^*, as a function of the driving voltage amplitude, ϕ_1. Discharge conditions: $p = 0.5$ Pa, $L = 6.7$ cm, $f = 13.56$ MHz, $N = 1$.

al [44] (based on a discharge model in which the same realistic model for the description of the electron-surface interaction was implemented as in the present work) for very similar discharge conditions: $p = 0.5$ Pa, $L = 6.7$ cm, $f = 13.56$ MHz, and $\phi_1 = 1000$ V. In [44], two beams of energetic electrons (and consequently, two separate maxima in the spatio-temporal distribution of the ionization rate) were found at both electrodes during an RF period: (i) strong ionization at the expanding sheath edge (beam I) and (ii) additional ionization during sheath collapse (beam II, weaker compared to beam I). Despite the similar discharge conditions, ionizing beams launched at the electrodes during sheath collapse are not found in the present study, only strong ionization at the expanding sheath edges can be observed. However, in the work of Horváth *et al* [44], a relatively high constant γ-coefficient of 0.4, appropriate for dielectric surfaces, was assumed and the parameters of the model for the electron-surface interaction were also different: SiO_2 surfaces were considered, characterized by significantly higher values for the maximum electron induced SEE at normal incidence, $\sigma_{\max,0}$ (2.5 vs 1.2 in the present study), and for the maximum of the elastic electron reflection, $\eta_{\mathrm{e,max}}$ (0.5 vs 0.1 in the present study). As both γ-electrons and the high δ-electron yields upon electron impact at low pressures and high voltage amplitudes were identified as important factors in the formation of the ionizing beams during sheath collapse, the lack of these beams in the present

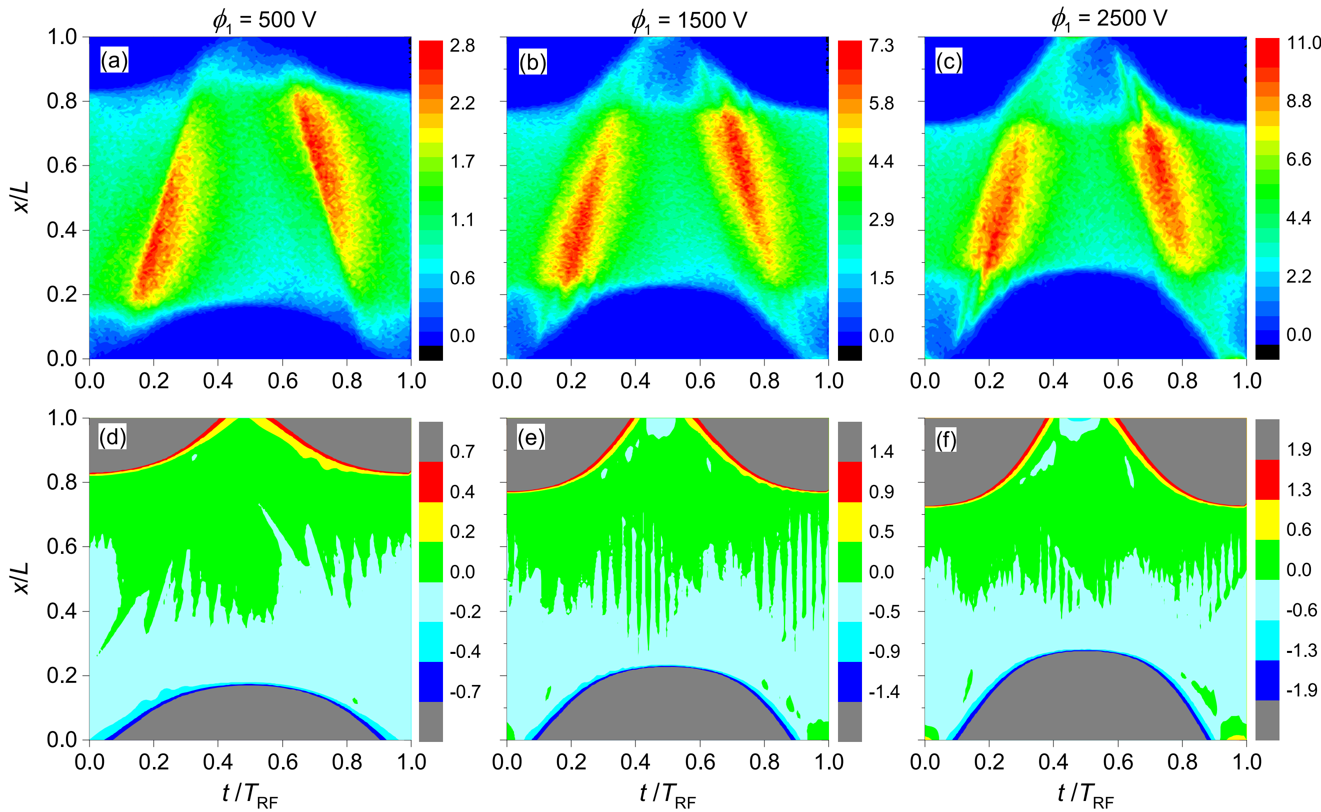

Figure 7. Spatio-temporal distribution of the ionization rate (top row, in units of 10^{20} m^{-3}s^{-1}) and the electric field (bottom row, in units of 10^4 Vm^{-1}, the scale is zoomed to small values) for different values of ϕ_1: $\phi_1 = 500$ V (first column), $\phi_1 = 1500$ V (second column) and $\phi_1 = 2500$ V (third column). The powered electrode is at $x/L = 0$, while the grounded electrode is at $x/L = 1$. $T_{\rm RF}$ indicates one period of the driving frequency. Discharge conditions: $p = 0.5$ Pa, $L = 6.7$ cm, $f = 13.56$ MHz, $N = 1$.

simulation results can be explained by the different characteristics of the electrode material and surface conditions (clean Cu electrodes) taken into account here both in the description of the electron-surface interaction, as well as in the description of the heavy-particle—surface interactions (resulting in low effective γ^* values). This explanation is supported by the simulation results presented in [45], which demonstrated that decreasing the (constant) γ-coefficient (from 0.4 to 0.0), as well as decreasing the voltage amplitude (from 1500 to 100 V) at low pressures (< 3 Pa) leads to vanishing of the beams of energetic electrons launched shortly before the time of sheath collapse at both electrodes. However, this work pointed out that δ-electrons can still contribute significantly to the ionization in the discharge at low voltages, as well as at low values of the γ-coefficient [45].

Figure 8 shows the individual contributions of δ-electrons (electron induced SEs), bulk electrons (electrons generated in electron or ion impact ionization processes), and γ-electrons (SEs induced by ions) to the total ionization rate obtained at $\phi_1 = 500$ V (first row) and $\phi_1 = 2500$ V (second row), shown in figures 7(a) and (c), respectively. At both voltage amplitudes, δ-electrons play an important role in the ionization dynamics. At $\phi_1 = 500$ V, 37% of the ionization is directly generated by δ-electrons (figure 8(a)), while at $\phi_1 = 2500$ V the most significant portion of the ionization, 52%, is induced by these electrons. The contribution of bulk electrons to the ionization is 58% and 42% at $\phi_1 = 500$ V and $\phi_1 = 2500$ V, respectively (figures 8(b) and (e)), while less than 5% of the total ionization is induced by γ-electrons (figures 8(c) and (f)). As some bulk electrons are generated by δ-electrons, there is an indirect effect of δ-electrons on the ionization dynamics accounted as ionization induced by bulk electrons. At the highest voltage amplitude of $\phi_1 = 2500$ V, about 2% of the ionization is induced by ions and fast neutrals.

In figure 9, various types of electron fluxes at the powered (left axes) and grounded (right axes) electrodes are shown. In the top row, results obtained for $\phi_1 = 500$ V are shown, while in the bottom row results for $\phi_1 = 2500$ V (the highest voltage amplitude applied in this study) are presented. In the first column, the flux of electrons reaching the electrode surfaces (IN e$^-$ flux) and the outgoing electron induced SE flux (OUT e$^-$ flux) can be seen at both electrodes. Here, IN and OUT denote directions relative to the electrode surfaces. The OUT e$^-$ fluxes comprise elastically reflected electrons, inelastically reflected electrons, and δ-electrons. While at $\phi_1 = 500$ V the OUT e$^-$ flux is significantly lower than the IN e$^-$ flux (figure 9(a)), at $\phi_1 = 2500$ V, the IN and OUT e$^-$ fluxes are similar at both electrodes (figure 9(d)). Under such conditions (in the presence of strong electron emission from the boundary surfaces), a reversed electric field is generated to enhance the electron transport to each electrode during sheath collapse in order to balance the ion and electron fluxes there on time average. Regions of field reversal can be seen in the spatio-temporal maps of the electric field in panels (e) and (f) of figure 7. In

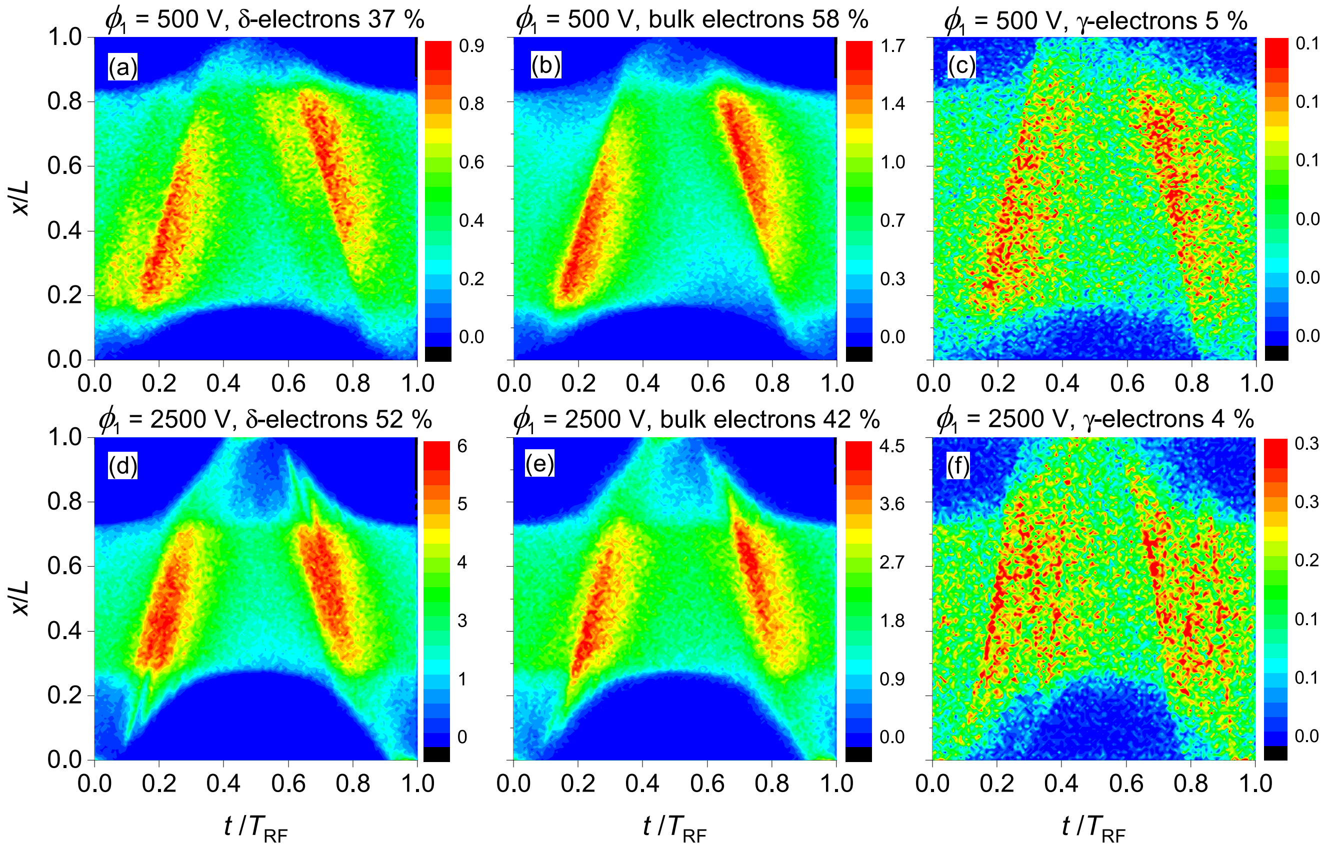

Figure 8. Spatio-temporal distribution of the contribution of δ-electrons (first column), bulk electrons (second column), and γ-electrons (third column) to the total ionization rate (shown in figures 7(a) and (c)) obtained for $\phi_1 = 500$ V (first row) and $\phi_1 = 2500$ V (second row). The powered electrode is at $x/L = 0$, while the grounded electrode is at $x/L = 1$. T_{RF} indicates one period of the driving frequency. The color scales are in units of 10^{20} m^{-3}s^{-1}. Discharge conditions: $p = 0.5$ Pa, $L = 6.7$ cm, $f = 13.56$ MHz, $N = 1$.

the second column of figure 9, the OUT e$^-$ fluxes (SE fluxes) shown in the panels in the first column are decomposed to the fluxes of reflected electrons (including elastically and inelastically reflected electrons) and the fluxes of electron induced SEs (δ-electrons) at both electrodes. The fluxes of heavy-particle induced SEs (γ-electrons) are also plotted in these panels ((b) and (e)). At both voltages, the SE flux induced by electrons is mainly composed of δ-electrons. The contributions of bulk electrons, δ-electrons, and γ-electrons (originated at the powered and grounded electrodes) to the generation of these SE fluxes (outgoing fluxes of δ-electrons) are shown in the third column of figure 9 for the two different voltage amplitudes. The generation of δ-electrons by the various electron groups at the grounded electrode is analyzed below (the same surface processes take place at the powered electrode half an RF period later), based on panels (c) and (f) of figure 9.

At $\phi_1 = 500$ V at the grounded electrode (see the top right axes in figure 9(c)), most δ-electrons are generated by bulk electrons, and δ-electrons created at both electrodes also have a significant contribution to the generation of δ-electrons during the time of sheath collapse at this electrode. Additionally, a low number of δ-electrons is created by γ-electrons (generated at both the powered and grounded electrodes) in this time period. At the higher voltage amplitude of $\phi_1 = 2500$ V (figure 9(f)), the contribution of δ-electrons (created at both the powered and grounded electrodes) to the emission of SEs increases and δ-electrons play a role comparable to bulk electrons in the generation of δ-electrons. The δ-electrons created this way induce significant ionization at the expanding sheath edge, and dominate the ionization dynamics at high voltage amplitudes (figure 8). δ-electrons behave similarly to bulk electrons. Many δ-electrons are generated during sheath collapse, when energetic electrons hit the electrode. These δ-electrons are emitted at low energies. When the sheath expands, they are 'kicked' in the same way as bulk electrons. At both voltages, additional δ-electrons are generated shortly before the time of sheath collapse ($0.3 < t/T_{\mathrm{RF}} < 0.4$) by δ- and γ-electrons created at the opposing (powered) electrode, as well as at the beginning of the sheath expansion phase ($0.6 < t/T_{\mathrm{RF}} < 0.8$) by γ-electrons created at the powered electrode. These δ-electrons, accelerated by the electric field in the sheath, further enhance the ionization in the discharge.

The contribution of the different electron groups (γ-electrons, δ-electrons, and bulk electrons) to the total ionization in the discharge as a function of the driving voltage amplitude is shown in figure 10. The direct contribution of γ-electrons to the ionization is less than 5% for all ϕ_1 at the low pressure of 0.5 Pa, which can be explained by the low values of γ^* obtained for clean Cu surfaces and the inefficient collisional multiplication of γ-electrons inside the sheaths under

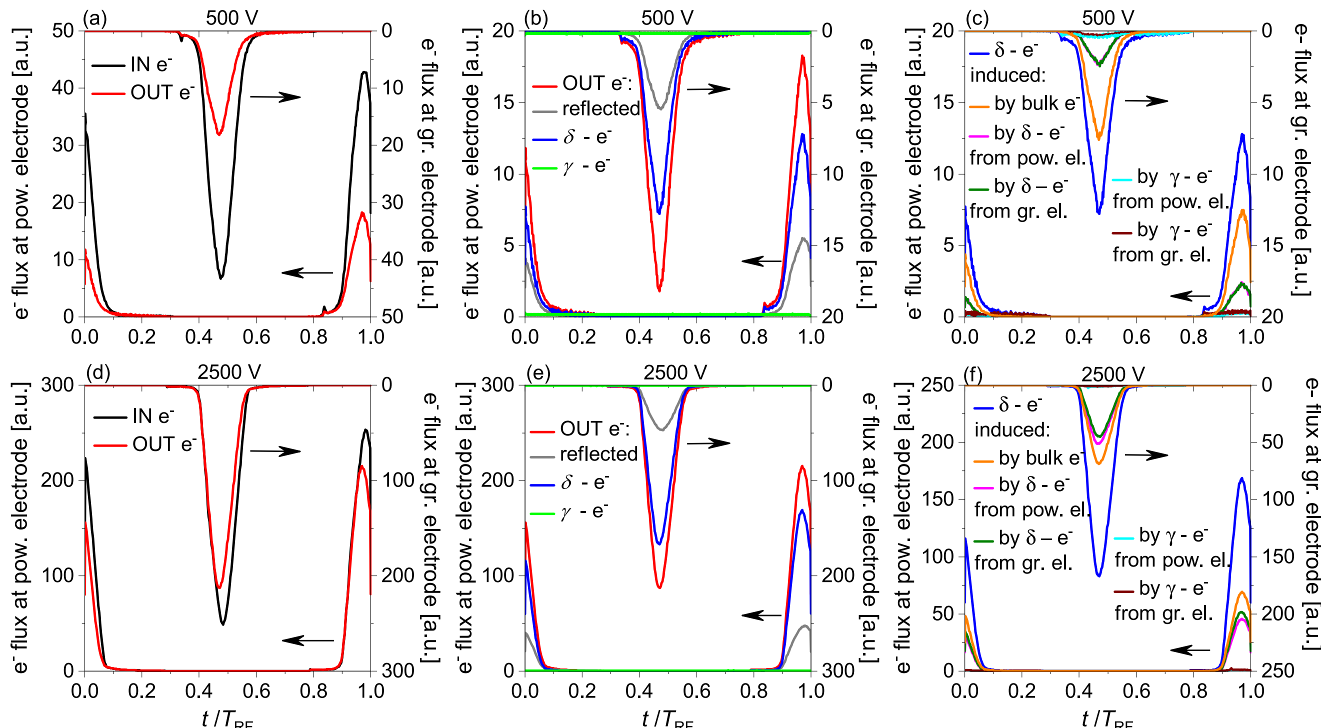

Figure 9. Fluxes of distinct electron groups at the electrode surfaces. Top row: $\phi_1 = 500$ V. Bottom row: $\phi_1 = 2500$ V. First column: flux of electrons reaching the electrodes (IN e^-) and electron induced total SE flux (OUT e^-) at the powered and grounded electrodes. Second column: electron induced total SE flux and its components (reflected electrons and δ-electrons) at the powered and grounded electrodes. The flux of heavy-particle induced SEs (γ-electrons) is also shown at both electrodes. Third row: the outgoing flux of δ-electrons and the contribution of bulk electrons, δ-electrons and γ-electrons (emitted at both electrodes) to the electron induced SEE. In each panel, the electron fluxes at the powered electrode are shown by the left scales, while those at the grounded electrode by the right scales. Discharge conditions: $p = 0.5$ Pa, $L = 6.7$ cm, $f = 13.56$ MHz, $N = 1$.

low pressure conditions. At $\phi_1 = 250$ V, δ-electrons have a contribution of 32% to the total ionization, which increases up to about 61% at $\phi_1 = 1750$ V, then slightly decreases towards higher values of ϕ_1 (their contribution to the ionization is about 50% at $\phi_1 = 2500$ V). A reverse trend can be observed for the dependence of the contribution of bulk electrons to the ionization on the applied voltage amplitude: it decreases from about 63% at $\phi_1 = 250$ V to 33% at $\phi_1 = 1750$ V, followed by a moderate increase at high voltage amplitudes. By increasing the voltage amplitude, more δ-electrons are created at the electrodes by energetic electrons, which can induce ionization. However, the electrons created as a result of electron impact ionization of the background Ar gas atoms by δ-electrons are considered bulk electrons (by definition) and the ionization induced by them is accounted for as contribution of bulk electrons to the ionization. The more ionization by δ-electrons is done, the larger number of bulk electrons are created, which can also induce ionization. As a consequence of these effects, at high voltage amplitudes (above $\phi_1 = 1750$ V) the contribution of δ-electrons to the ionization decreases, while that of bulk electrons increases. The ionization induced by these bulk electrons represents an indirect effect of δ-electrons on the ionization dynamics.

These results confirm that δ-electrons can have a strong influence on the discharge parameters in CCPs at low pressures and high voltages. It is noted that δ-electrons have a direct contribution of about 30% to the total ionization even at the lowest voltage amplitude of 250 V considered here. Moreover, these results were obtained by describing the heavy-particle induced SEE realistically in the discharge model (assuming clean metal surfaces), resulting in low values of the self-consistently calculated effective SEEC, γ^*. This shows that the SEE induced by electrons is an important process and δ-electrons can play an important (even dominant) role in the ionization dynamics also in case of surfaces characterized by low SE yields due to heavy-particle impact.

3.2. Multi-frequency driving voltage waveforms

In this section, simulation results for Ar discharges with Cu electrodes, driven by multiple harmonics $1 \leqslant N \leqslant 4$ of the fundamental frequency of $f = 13.56$ MHz are presented. The driving voltage waveform is tailored by varying the phase angles of the even harmonics, θ ($\theta = \theta_2 = \theta_4$). The phase angles of the odd harmonics are set to 0° ($\theta_1 = \theta_3 = 0°$). The gap length, the pressure and the total voltage amplitudes are fixed at $L = 6.7$ cm, $p = 0.5$ Pa and $\phi_{\rm tot} = 1000$ V.

By applying more than one harmonic to drive the discharge, a dc self-bias develops. In figure 11, the dc self-bias voltage is shown as a function of the identical phase angle of the even harmonics, θ, for different numbers of applied harmonics, N. The dc self-bias can be tuned by changing θ: at $N = 2$, it changes from −470 to 470 V by varying θ from 0° to 180°, while at $N = 4$, it changes from −540 to 540 V.

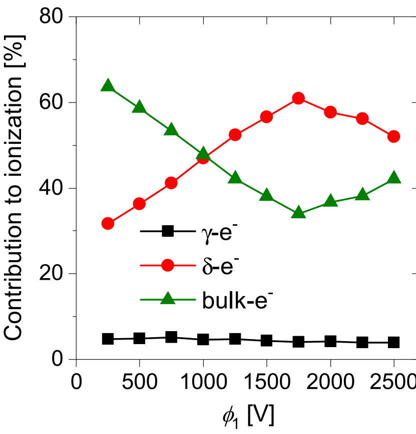

Figure 10. The contribution of different electron groups to the total ionization as a function of the driving voltage amplitude, ϕ_1. Discharge conditions: $p = 0.5$ Pa, $L = 6.7$ cm, $f = 13.56$ MHz, $N = 1$.

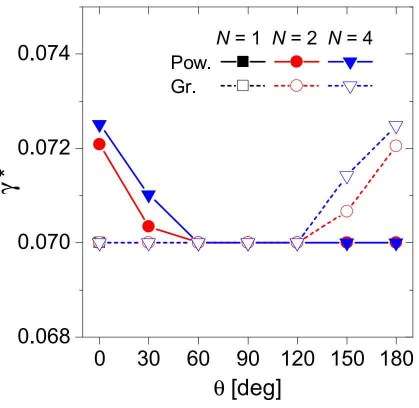

Figure 12. The effective SEEC, γ^*, as a function of the phase angle(s) of the even harmonics, θ, at the powered and grounded electrodes for different numbers of applied harmonics, N. Discharge conditions: $p = 0.5$ Pa, $L = 6.7$ cm, $f = 13.56$ MHz, $\phi_{\rm tot} = 1000$ V. Note that the symbols completely overlap in some cases.

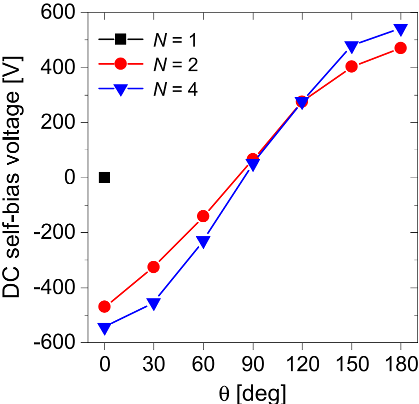

Figure 11. The dc self-bias voltage as a function of the phase angle(s) of the even harmonics, θ, for different numbers of applied harmonics, N. Discharge conditions: $p = 0.5$ Pa, $L = 6.7$ cm, $f = 13.56$ MHz, $\phi_{\rm tot} = 1000$ V.

The variation of the dc self-bias by changing the phase angles affects the energy of ions arriving at the electrodes [17]. As fast neutrals are created via elastic collisions between Ar^+ ions and atoms of the background gas in the sheaths, the energy of Ar^f atoms at the electrodes is also affected (indirectly) by the dc self-bias voltage. Due to the dependence of the various surface processes on the particle energies, varying the dc self-bias via θ is expected to influence the efficiency of those surface processes (e.g. SE yield, sputtering yield) in which heavy-particles are involved.

In a recent PIC/MCC simulation study of low-pressure Ar discharges driven by TVWs (in which the heavy-particle induced SEE was described realistically, while the electron induced SEE was neglected, and both 'clean' and 'dirty' metal surface conditions [73] were considered), it was shown that the self-consistently calculated effective SEEC, γ^*, changes by tuning the phase angle of the driving harmonics, θ [49]. This was explained by the variation of the heavy-particle energies, and consequently the variation of the energy-dependent SE yields due to these particles as a function of θ. Under the conditions investigated here, changing the phase angle(s) of the driving harmonics only slightly affects γ^*. For all N and θ, γ^* is about $\sim$0.07 at both electrodes (slightly higher-up to 3% higher than 0.07-values of γ^* are found at $\theta < 60°$ at the powered electrode, and for $\theta > 120°$ at the grounded electrode), as it can be seen in figure 12.

The mean energies of Ar^+ ions and Ar^f atoms at both electrodes as a function of θ are shown in the first column of figure 13 for different numbers of applied harmonics. By changing θ, the mean heavy-particle energies at the electrodes can be controlled. The mean energy of Ar^+ ions (figure 13(a)) is increased at the grounded electrode by a factor of about 7 at $N = 4$ (from about 80 eV up to about 560 eV) and decreased at the powered electrode by changing θ from 0° to 180°; at $N = 2$, the mean energy of Ar^+ ions is changed by a factor of about 4 at both electrodes (between 130 and 530 eV). Similarly, in case of fast neutrals, the mean energy of Ar^f particles (figure 13(d)) is increased at the grounded electrode by a factor of about 5.4 at $N = 4$ (from about 45 to 245 eV) and decreased at the powered electrode by changing θ from 0° to 180°; at $N = 2$, the mean energy of Ar^f atoms is changed by a factor of about 3.3 at both electrodes (between 70 and 230 eV) by changing θ.

At the grounded electrode, for values of θ below 120°, the Ar^+ ion energies are below 500 eV for all N (see the mean Ar^+ ion energies in figure 13(a) and the flux-energy distribution of Ar^+ ions at the grounded electrode for $N = 4$, $\theta = 0°$ and $\theta = 90°$ in figure 14(a)). The SE yield for Ar^+ impact on clean metal surfaces is 0.07 for these particle energies (figure 2(a)). Under these conditions Ar^f atoms do not contribute significantly to the SEE, due to their lower particle energies (figures 13(d) and 14(b)) and lower fluxes (figure 13(e)) compared to those of Ar^+ at the electrodes. Therefore, γ^* is 0.07 at these phase angles at the grounded electrode for all N (figure 12). For $\theta > 120°$, there are Ar^+ ions with energies higher than 500 eV reaching the grounded electrode (see the mean Ar^+ ion energies in figure 13(a) and the flux-energy distribution of Ar^+ ions at the grounded electrode for $N = 4$ and $\theta = 180°$ in figure 14(a)). The SE yields

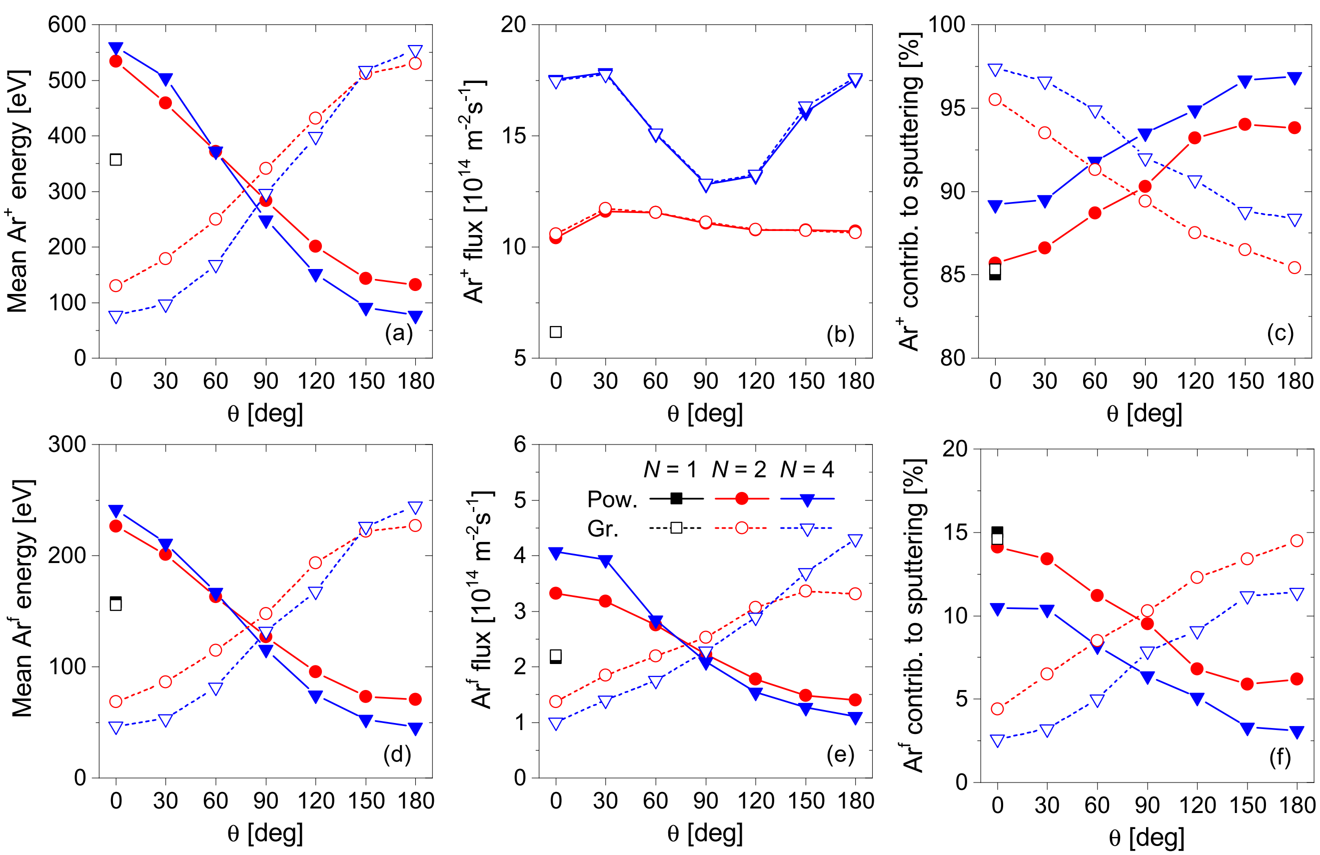

Figure 13. The mean energy (first column) and flux (second column) of Ar^+ ions (first row) and Ar^f neutrals (second row) at the electrodes, as well as their contribution to the sputtering of the Cu electrodes (third column) for different numbers of applied harmonics, *N*, as a function of the phase angle(s), θ. Only atoms with energy above 23 eV are taken into account as Ar^f. Discharge conditions: $p = 0.5$ Pa, $L = 6.7$ cm, $f = 13.56$ MHz, $\phi_{tot} = 1000$ V. Note that the symbols completely overlap in some cases. The legend in panel (e) applies to all panels.

due to these ions are higher than 0.07 (figure 2(a)). Therefore, γ^* computed based on equation (4) is slightly higher than 0.07 at these phase angles at the grounded electrode for $N = 2$ and $N = 4$ (figure 12). Similarly, at the powered electrode, for $\theta < 60^\circ$, Ar^+ ions with energies higher than 500 eV are the reason for γ^* values slightly above 0.07 for $N = 2$ and $N = 4$, while for $\theta \geqslant 60^\circ$ $\gamma^* = 0.07$ for all *N* (see the flux-energy distribution of Ar^+ ions and Ar^f atoms at the powered electrode in panels (d) and (e) of figure 14 for different values of θ).

At such energies of Ar^+ ions and Ar^f atoms at the electrodes, significant sputtering of the Cu electrodes is induced by these particles (see figure 14). Under the studied discharge conditions most of the sputtering is induced by Ar^+ ions. They have a contribution to the total sputtering above 85% for all *N* and θ (figure 13(c)), while 5% to 15% of the total sputtering is induced by Ar^f atoms (figure 13(f)). By increasing the number of applied harmonics at a given θ, the contribution of Ar^+ ions to the sputtering increases, while that of Ar^f atoms decreases at both electrodes. The flux of Ar^f atoms decreases at the powered electrode and increases at the grounded electrode by changing θ from 0° to 180°, for $N > 1$ (figure 13(e)). This is due to the variation of the width of the sheath region where fast atoms are created by Ar^+ ions as a function of θ at both electrodes (see later in figure 17). This effect, combined with the variation of the energy of Ar^f atoms as a function of θ, results in a decrease of the contribution of Ar^f atoms to the sputtering at the powered electrode and an increase of their contribution to the sputtering at the grounded electrode as θ is changed from 0° to 180° at $N = 2$ and $N = 4$. As a consequence of this, the contribution of Ar^+ ions to the sputtering increases at the powered electrode and decreases at the grounded electrode as θ is increased (figure 13(c)). Note the equal fluxes of Ar^+ ions at the two electrodes for all θ and *N* due to the nonlocal ionization dynamics (symbols overlap in figure 13(b)).

By tuning the control parameter for the heavy-particle energies, θ, the flux of sputtered Cu atoms at the electrodes is affected at both electrodes. This is illustrated in panels (c) and (f) of figure 14, which show the flux-energy distribution of sputtered Cu atoms at the grounded and powered electrodes, respectively, for $N = 4$ harmonics and different values of the θ phase angle: 0°, 90°, and 180°. At the grounded electrode, the efficiency of the sputtering can be enhanced and the flux of sputtered Cu atoms can be increased by increasing θ (figure 14(c)). The reverse scenario takes place at the powered electrode, where the highest sputter flux is obtained at $\theta = 0^\circ$ and the flux of sputtered Cu atoms decreases by increasing θ (figure 14(f)). At $N = 2$, the sputtered Cu flux can be increased/decreased by a factor of about 3 at the grounded/powered electrode by changing θ from 0° to 180° (figure 15). At $N = 4$, compared to the case of $\theta = 0^\circ$, 5 times higher/lower sputtered Cu fluxes can be obtained at the grounded/powered electrode by increasing θ to 180°. These

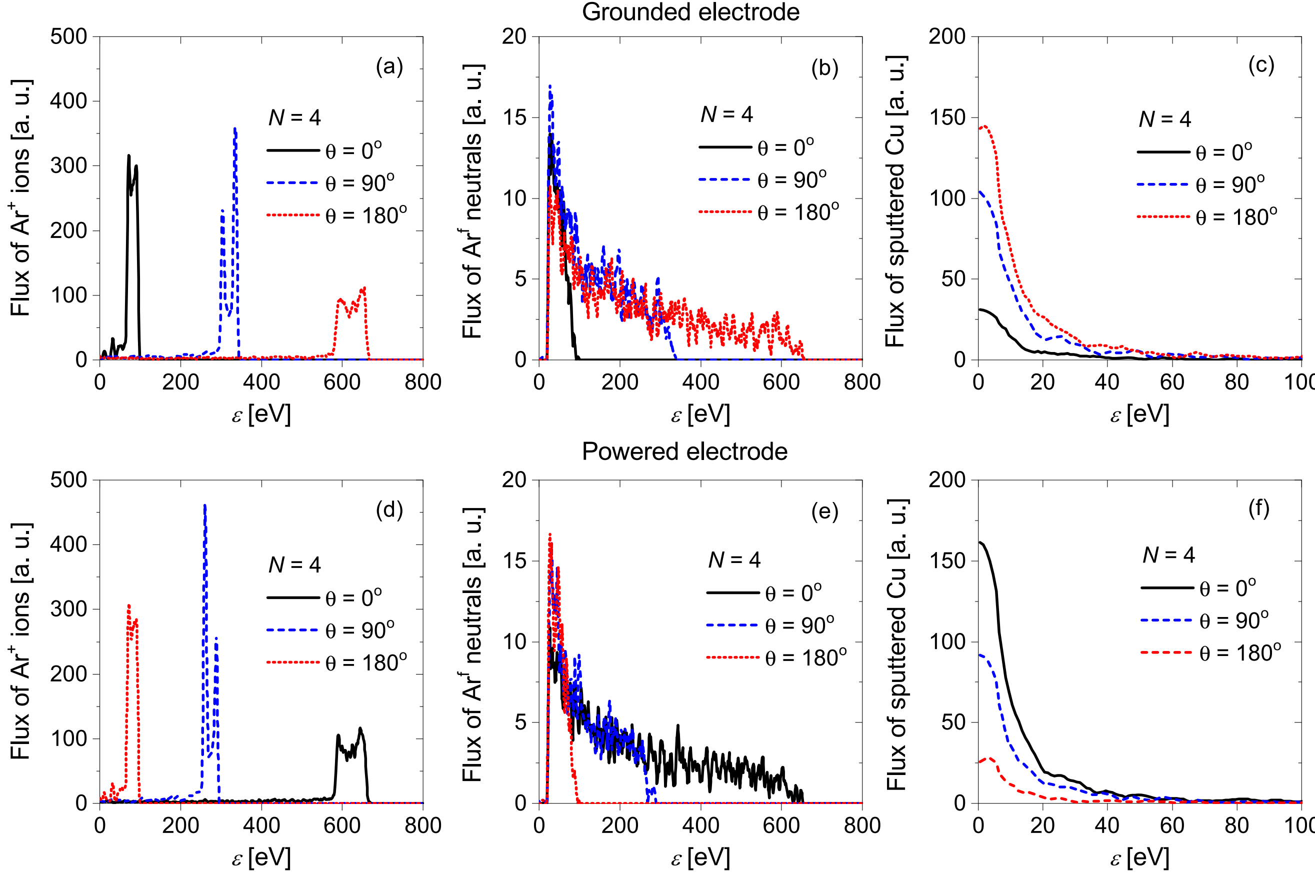

Figure 14. Flux-energy distribution of Ar^+ ions (first column), Ar^f atoms (second column) and sputtered Cu atoms (third column) at the grounded (top row) and powered (bottom row) electrodes as a function of the ion/atom energy, ε, for $N = 4$ harmonics, for different values of θ. The vertical scales are in arbitrary units and can be compared to each other. Discharge conditions: $p = 0.5$ Pa, $L = 6.7$ cm, $f = 13.56$ MHz, $\phi_{tot} = 1000$ V.

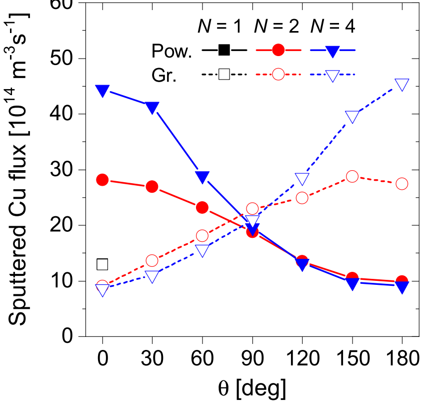

Figure 15. The (outgoing) flux of sputtered Cu atoms at both electrodes as a function of θ for different numbers of applied harmonics, N. Discharge conditions: $p = 0.5$ Pa, $L = 6.7$ cm, $f = 13.56$ MHz, $\phi_{tot} = 1000$ V. Note that the symbols completely overlap in some cases, e.g. at $N = 1$.

results show that the flux of sputtered atoms can be controlled by θ at both electrodes in multi-frequency discharges driven by TVWs. At $\theta = 90°$, the flux of sputtered atoms is similar at both electrodes. At $\theta = 0°$, the sputter flux is high at the powered electrode and low at the grounded electrode (a factor of 3 difference at $N = 2$, and a factor of 5 difference at $N = 4$), while at $\theta = 180°$ the Cu flux is high at the grounded electrode and low at the powered electrode (figure 15).

Figure 16 shows the time-averaged density distributions of various plasma species in the discharge gap for different values of θ at $N = 4$, including the density of sputtered Cu atoms. At $\theta = 90°$, the Cu atoms are uniformly distributed within the gap (net sources of Cu atoms are equal at both electrodes). At $\theta = 0°$ and $\theta = 180°$, the density of sputtered atoms is slightly different at the two electrodes: at $\theta = 0°$ the Cu density at the powered electrode is about 10% higher compared to that at the grounded electrode; at $\theta = 180°$, a higher sputtered atom density is found at the grounded electrode compared to the powered electrode. This can be explained by the different net sources of Cu atoms at both electrodes due to the discharge asymmetry at $\theta = 0°$ and $\theta = 180°$.

Figure 17 shows the spatio-temporal plots of the ionization rate and the electric field for $N = 4$ harmonics, for different phase angles, θ ($\theta = 0°, 90°$, and $180°$). For all θ, the discharge operates in the α-mode. At $\theta = 0°$, the spatio-temporal distribution of the ionization is strongly asymmetric (figure 17(a)): strong α-mode ionization, enhanced by non-linear electron resonance heating (NERH) [55, 116–119] is found only at the powered electrode. In such low pressure plasmas, the nonlinear interaction of bulk electrons with the expanding sheath leads to the formation of multiple energetic electron beams

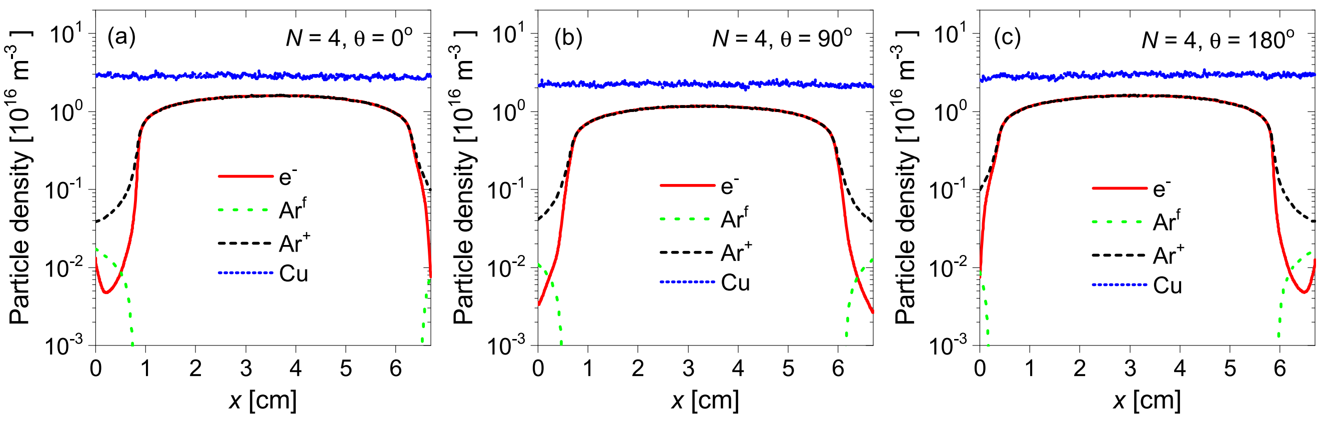

Figure 16. Time-averaged density distributions of heavy-particles and electrons in the discharge gap for $N = 4$ harmonics, for different values of θ: (a) $\theta = 0°$, (b) $\theta = 90°$ and (c) $\theta = 180°$. Discharge conditions: $p = 0.5$ Pa, $L = 6.7$ cm, $f = 13.56$ MHz, $\phi_{\mathrm{tot}} = 1000$ V.

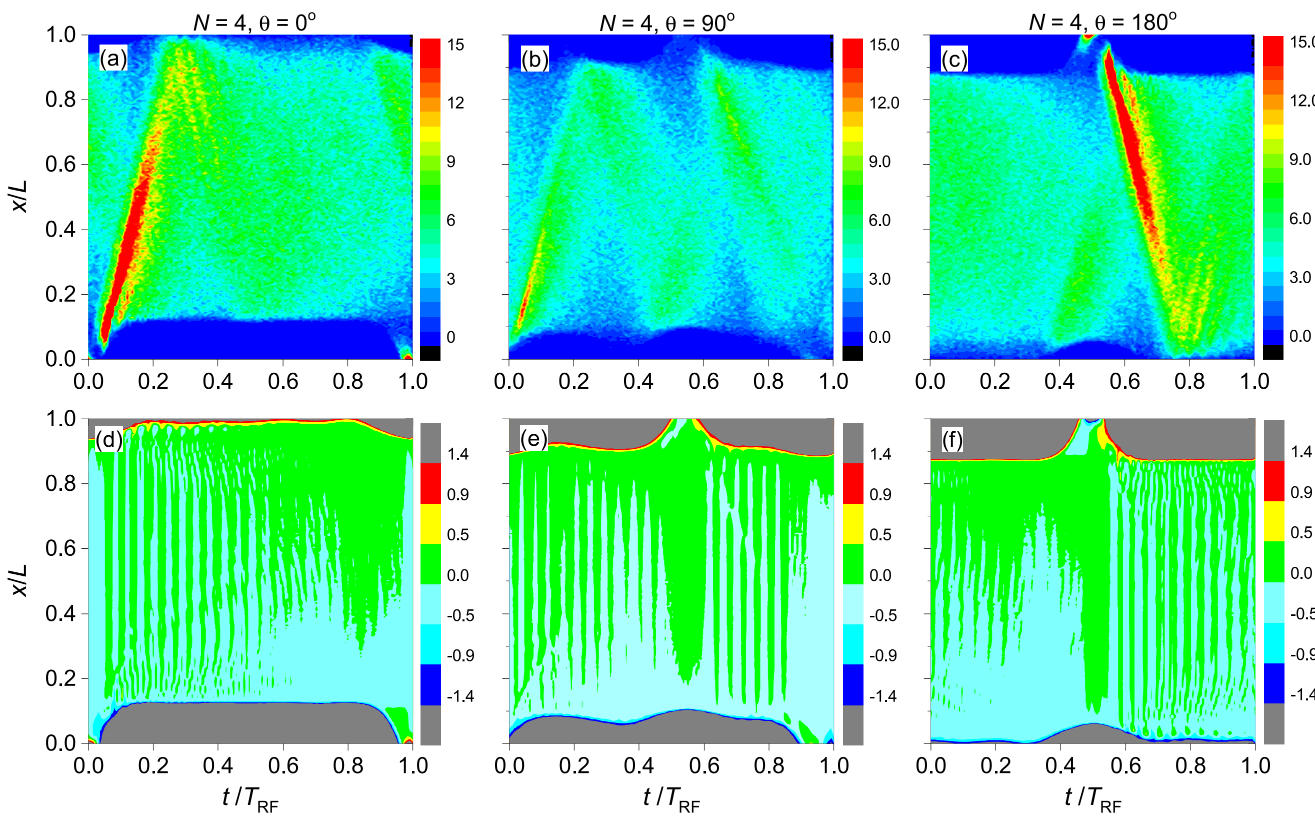

Figure 17. Spatio-temporal distribution of the ionization rate (top row, in units of 10^{20} m^{-3}s^{-1}) and the electric field (bottom row, in units of 10^4 Vm^{-1}, the scale is zoomed to small values) for $N = 4$ applied harmonics, for different phase angles: $\theta = 0°$ (first column), $\theta = 90°$ (second column), and $\theta = 180°$ (third column). The powered electrode is at $x/L = 0$, while the grounded electrode is at $x/L = 1$. T_{RF} indicates one period of the fundamental frequency. Discharge conditions: $p = 0.5$ Pa, $L = 6.7$ cm, $f = 13.56$ MHz, $\phi_{\mathrm{tot}} = 1000$ V.

which propagate into the plasma bulk and induce significant ionization [120–124]. Similar ionization dynamics can be seen half a period later (the period of the fundamental frequency is T_{RF}) at the grounded electrode for $\theta = 180°$ (figure 17(c)). At $\theta = 90°$ the spatio-temporal distribution of the ionization is more symmetric (figure 17(b)). At this phase angle, the ionization maxima are significantly weaker than those obtained for $\theta = 0°$ and $\theta = 180°$, and less ionization is produced on time and space average compared to $\theta = 0°$ and 180°. This leads to lower Ar^+ ion fluxes to the electrodes at $\theta = 90°$ compared to those at $\theta = 0°$ and $\theta = 180°$ (see figure 13(b) for $N = 4$).

The SEE due to heavy-particle impact is not strong under these conditions (see the low values of the self-consistently calculated γ^* effective SEEC in figure 12). Therefore, γ-electrons only moderately enhance the ionization in the discharge. Most of the ionization is induced by δ-electrons and bulk electrons, as it can bee seen in figure 18. This figure shows the contribution of δ-electrons, bulk electrons, and γ-electrons to the total ionization obtained for $N = 4$ applied

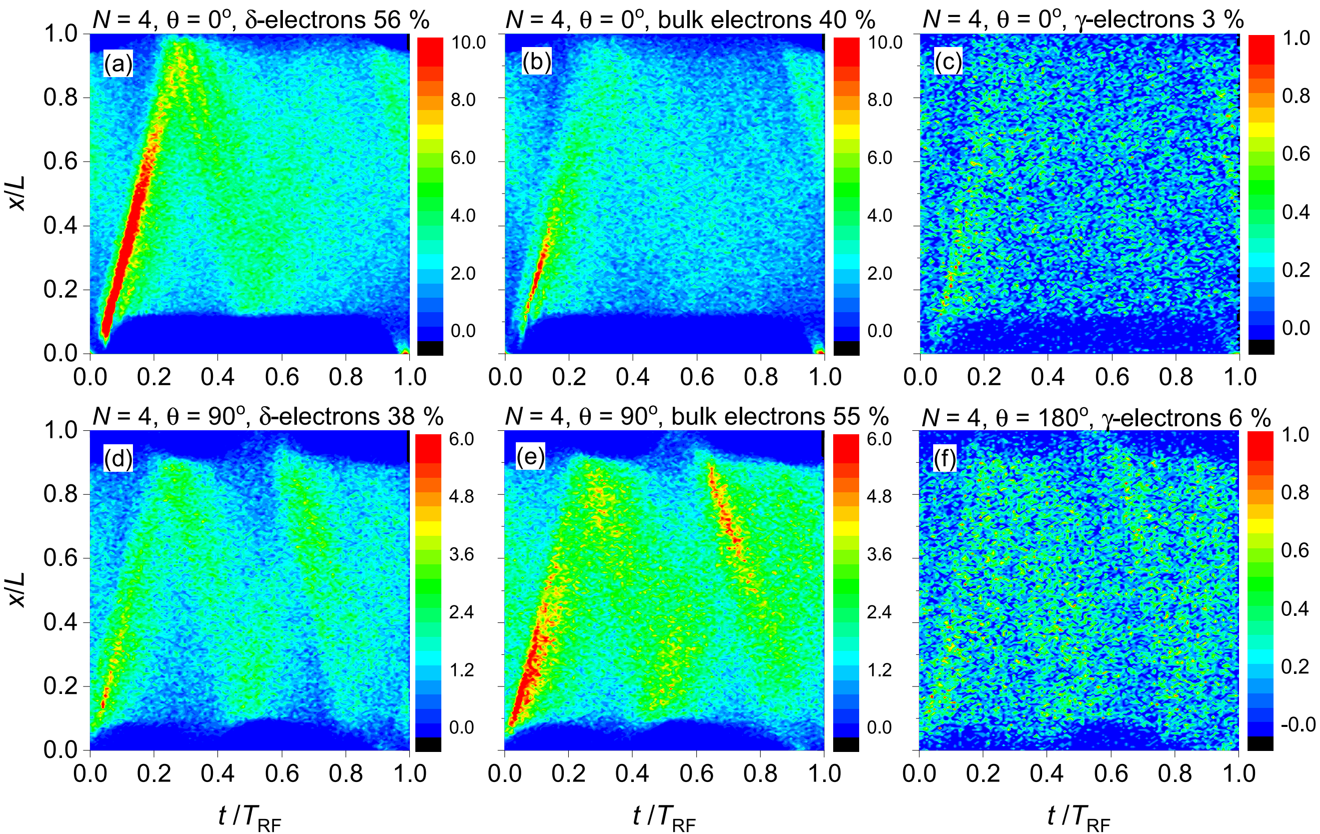

Figure 18. Spatio-temporal distribution of the contribution of δ-electrons (first column), bulk electrons (second column), and γ-electrons (third column) to the total ionization rate (shown in figures 17(a) and (b)) obtained for $N = 4$, $\theta = 0°$ (first row) and $\theta = 90°$ (second row). The powered electrode is at $x/L = 0$, while the grounded electrode is at $x/L = 1$. T_{RF} indicates one period of the fundamental frequency. The color scales are in units of 10^{20} m^{-3}s^{-1}. Discharge conditions: $p = 0.5$ Pa, $L = 6.7$ cm, $f = 13.56$ MHz, $\phi_{\mathrm{tot}} = 1000$ V.

harmonics at $\theta = 0°$ and $\theta = 90°$. At $\theta = 0°$, 56% of the total ionization is directly induced by δ-electrons, while bulk electrons have a contribution of about 40%. The contribution of γ-electrons to the total ionization is low, 3% of the total. 1% of the ionization is induced by ions and fast atoms. At this phase angle, the sheath is expanded for a long fraction of the period of the fundamental frequency (T_{RF}) at the powered electrode and it is collapsed for a long fraction of T_{RF} at the grounded electrode. The asymmetry of the discharge affects the ionization induced by SEs. During the time of sheath collapse at the powered electrode a high number of δ-electrons are emitted (see the high flux of δ-electrons in the left scale of figure 19(b) at $0.0 \leqslant t/T_{\mathrm{RF}} < 0.05$ and $0.95 \leqslant t/T_{\mathrm{RF}} < 1.0$). These δ-electrons are mainly induced by bulk electrons. δ-electrons created at both electrodes also induce significant SEE in this time interval, while γ-electrons (from both electrodes) have only a minor contribution to the emission of true SEs (figure 19(c)). Under these conditions, in order to compensate the ion flux, a reversed electric field develops (with maximum value of about 290 Vcm^{-1}) to facilitate the electron transport to the electrode during sheath collapse (figure 17(d)). Due to this, some of the δ-electrons emitted at the powered electrode are pulled back to the electrode where they can induce additional SEE. The δ-electrons emitted at the powered electrode induce strong ionization at the expanding sheath edge at the powered electrode. At low pressures, some of these δ-electrons can reach the grounded electrode during the long period of sheath collapse at this electrode, where they can induce additional emission of δ-electrons, like bulk electrons and δ-electrons previously created at the grounded electrode (see the contributions of various electron groups to the emission of δ-electrons at the grounded electrode in the right scale of figure 19(c)). Note the oscillations of the electron fluxes (both incoming and outgoing fluxes) at the grounded electrode seen in the right scales of panels (a)–(c) of figure 19 due to multi-beams formed under NERH [55, 116–119] at the powered electrode. The δ-electrons emitted at the grounded electrode at $0.1 \leqslant t/T_{\mathrm{RF}} < 0.4$ induce significant ionization in the bulk (figure 18(a)). This beam of δ-electrons, being reflected from the expanded sheath at the powered electrode, induces emission of δ-electrons at the grounded electrode at $0.7 \leqslant t/T_{\mathrm{RF}} < 0.9$ (right scale in figure 19(b)). At $\theta = 0°$ the bulk electrons also induce strong ionization at the expanding sheath at the powered electrode (figure 18(b)). However, most of these electrons are lost at the grounded electrode, where they can also induce emission of δ-electrons (figure 19(c)). Similarly, the γ-electrons emitted at the powered electrode when the sheath is expanded at $\theta = 0°$ are mainly lost at the other electrode where the sheath is collapsed for a long fraction of T_{RF}. These γ-electrons have a limited influence on the ionization dynamics, due to the low number of γ-electrons as a result

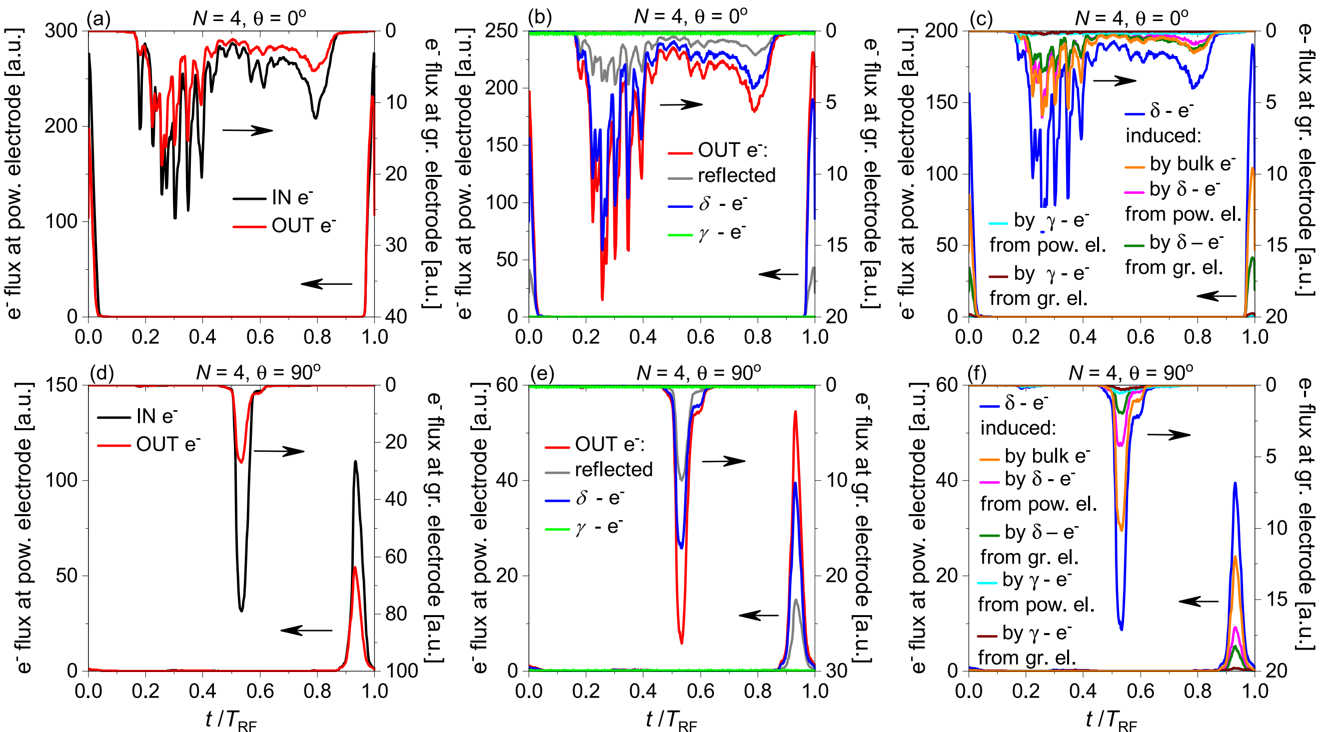

Figure 19. Top row: $N = 4$, $\theta = 0°$. Bottom row: $N = 4$, $\theta = 90°$. First column: electron flux to the electrodes (IN e^-) and electron-induced total SE flux (OUT e^-) at the powered and grounded electrodes. Second column: electron-induced total SE flux and its components (reflected electrons and δ-electrons) at the powered and grounded electrodes. The flux of heavy-particle induced SEs (γ-electrons) is also shown at both electrodes. Third row: the outgoing flux of δ-electrons and the contribution of bulk electrons, δ-electrons and γ-electrons (emitted at both electrodes) to the electron induced SEE. In each panel, the electron fluxes at the powered electrode are shown by the left scales, while those at the grounded electrode by the right scales. Discharge conditions: $p = 0.5$ Pa, $L = 6.7$ cm, $f = 13.56$ MHz, $\phi_{tot} = 1000$ V.

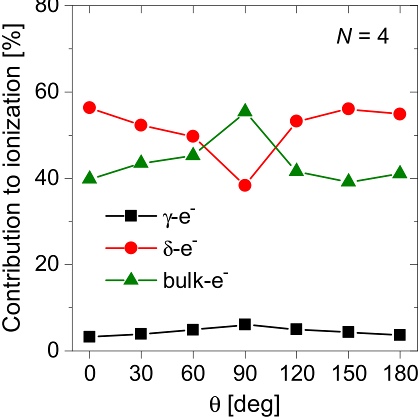

Figure 20. The contribution of different electron groups to the ionization as a function of the phase angles, θ, for $N = 4$ harmonics. Discharge conditions: $p = 0.5$ Pa, $L = 6.7$ cm, $f = 13.56$ MHz, $\phi_{tot} = 1000$ V.

of the low γ^*, their inefficient multiplication at low pressures, and their poor confinement (figure 18(c)).

At $\theta = 90°$, due to the high sheath voltages at both electrodes during a long fraction of T_{RF}, a good confinement of both bulk electrons (figure 18(e)) and γ-electrons (figure 18(f)) is found. Under these conditions the ionization is dominated by bulk electrons (55% of the total ionization) and the ionization generated by γ-electrons is also enhanced (6% of the total ionization compared to 3% at $\theta = 0°$). Again, about 1% of the ionization is induced by ions and fast atoms. At this phase angle, δ-electrons are emitted mainly at $0.85 \leqslant t/T_{RF} < 1.0$ at the powered electrode and at $0.45 \leqslant t/T_{RF} < 0.6$ at the grounded electrode and induce significant ionization in the discharge (38% of the total ionization, see figure 18(d)). At both electrodes, bulk electrons and δ-electrons (from both electrodes) have the highest contributions to the generation of δ-electrons (figure 19(f)). The fluxes of δ-electrons emitted at both electrodes are significantly lower at $\theta = 90°$ compared to $\theta = 0°$ (especially at the powered electrode, see figure 19(f) compared to figure 19(c)). As a result of this, their contribution to the total ionization is lower at $\theta = 90°$ compared to $\theta = 0°$. This can be seen in figure 20, which shows the contributions of the different electron groups (γ-electrons, δ-electrons, bulk electrons) to the total ionization as a function of the phase angle for $N = 4$ applied harmonics. The ionization directly induced by δ-electrons is at least 38% of the total ionization at $N = 4$. This increases to about 55% at phase angles $\theta = 0°$ and 180°, where they compensate the less efficient ionization induced by bulk electrons and γ-electrons (due to their poor confinement at these phase angles). Compared to the case of δ-electrons, an inverse trend can be observed in case of bulk electrons: the ionization induced by bulk electrons increases from about 40% at $\theta = 0°$ up to 55% at $\theta = 90°$, then decreases towards higher values of θ. The contribution of γ-electrons to the total ionization follows the trend seen in the case of the bulk electrons, however, their contribution remains below 10%

at all values of θ (3% at $\theta = 0°$ and 180°, and maximum 6% at $\theta = 90°$). Similar results are obtained for $N = 2$ (not shown in figure 20).

4. Conclusions

Particle-in-cell/Monte Carlo collisions (PIC/MCC) simulations were performed to investigate surface processes such as sputtering and secondary electron emission (SEE) in geometrically symmetric capacitively coupled Ar discharges with Cu electrodes driven by tailored voltage waveforms (TVWs). The driving voltage waveform was composed of a maximum of four consecutive harmonics of the fundamental frequency ($f = 13.56$ MHz), and was tailored by adjusting the phases of the even harmonics, θ. In all simulations, the gap length and the pressure were fixed at $L = 6.7$ cm and $p = 0.5$ Pa.

The simulations were based on a discharge model in which realistic approaches were implemented for the description of the SEE induced by electrons and heavy-particles (ions and fast neutrals) at the electrodes, as well as for the sputtering of the electrode by heavy-particles. The sputtering process and the role of SEs (focusing on electron induced SEs, i.e. δ-electrons) in the ionization dynamics was analyzed in case of applying a single harmonic ($N = 1$) excitation with different voltage amplitudes (250 V $\leqslant \phi_1 \leqslant$ 2500 V), followed by a study for multi-frequency driving voltage waveforms ($1 \leqslant N \leqslant 4$) at a fixed total voltage amplitude ($\phi_{\mathrm{tot}} = 1000$ V).

In single-frequency discharges, the flux of sputtered Cu atoms at the electrodes was found to increase by increasing the voltage amplitude, ϕ_1, from 250 to 2500 V (the Cu density remained by about three orders of magnitude lower than the density of the background Ar gas at 0.5 Pa at all ϕ_1). Under the conditions investigated here, most sputtering was caused by Ar^+ ions, corresponding to a contribution to the sputtering between 79% and 91% (slightly decreasing towards higher ϕ_1), while the sputtering induced by Ar^f atoms was between 9% and 21% (slightly increasing towards higher ϕ_1). δ-electrons were found to induce strong ionization in the α-mode at the expanding sheath edge and to dominate the ionization dynamics at high voltage amplitudes. At $\phi_1 = 1750$ V, their contribution to the total ionization was about 60%. A significant contribution of δ-electrons to the ionization was obtained even at the lowest voltage amplitude of 250 V considered here, about 30% of the total. The contribution of bulk electrons to the ionization decreased from about 63% at $\phi_1 = 250$ V to 33% at $\phi_1 = 1750$ V, followed by a moderate increase at high voltage amplitudes. Low values of the self-consistently calculated effective SEEC, γ^*, were obtained for all ϕ_1 ($0.07 \leqslant \gamma^* < 0.082$). The ionization induced directly by γ-electrons was less than 5% for all voltages.

By applying more than one harmonic ($2 \leqslant N \leqslant 4$) to drive the discharge, a dc self-bias was generated, which could be controlled efficiently by changing the phase angle(s) of the even harmonics, θ. By adding more harmonics to the driving voltage waveform, the interval over which the dc self-bias can be controlled was enlarged. The simulations showed that the mean energy of Ar^+ ions and Ar^f atoms at the electrodes can be controlled by θ, under all conditions investigated here. By changing θ from 0° to 180°, the mean energy of Ar^+ ions and Ar^f atoms was found to increase at the grounded electrode and to decrease at the powered electrode. Due to the dependence of the SEE and the sputtering induced by heavy-particles on the particle energies, varying θ was found to influence the efficiency of these surface processes. By tuning the control parameter for the heavy-particle energies, θ, the flux of sputtered Cu atoms was affected at both electrodes: the Cu atom flux increased at the grounded electrode and decreased at the powered electrode by varying θ from 0° to 180°. At $N = 2$, the sputtered Cu flux could be increased/decreased by a factor of about 3 at the grounded/powered electrode by increasing θ. At $N = 4$, compared to the case of $\theta = 0°$, 5 times higher/lower sputtered Cu fluxes were obtained at the grounded/powered electrode at $\theta = 180°$. Under these conditions, most of the ionization was induced by δ-electrons and bulk electrons. The ionization directly induced by δ-electrons was between 38% and 55% of the total at $N = 4$ (maximum at $\theta = 0°$ and 180°, minimum at $\theta = 90°$), while the ionization induced by bulk electrons increased from about 40% at $\theta = 0°$ up to 55% at $\theta = 90°$, then decreased towards higher values of θ. These results were obtained at low values of the self-consistently calculated effective SEEC, γ^*, characterizing clean metal surfaces. For all N and θ considered here, the SEE due to heavy-particle impact was found to be weak, values of γ^* about $\sim$0.07 were obtained at both electrodes. A further increase of the importance of δ-electrons in the ionization dynamics in multi-frequency discharges driven by TVWs is expected in case of surfaces characterized by high SE yields due to heavy-particle and electron impact (e.g. dielectric surfaces).

Acknowledgments

This work was supported by the US NSF Grant No PHY. 1601080, by the Hungarian National Research, Development and Innovation Office via grants K-119357, PD-121033 and FK-128924, by the German Research Foundation (DFG) within the frame of the collaborative research centre SFB-TR 87 (project C1), by the J Bolyai Research Fellowship of the Hungarian Academy of Sciences, and by the ÚNKP-19-3 New National Excellence Program of the Ministry for Innovation and Technology.

ORCID iDs

A Derzsi https://orcid.org/0000-0002-8005-5348
B Horváth https://orcid.org/0000-0002-2371-2444
Z Donkó https://orcid.org/0000-0003-1369-6150
J Schulze https://orcid.org/0000-0001-7929-5734

References

[1] Lieberman M A and Lichtenberg A J 2005 *Principles of Plasma Discharges and Materials Processing* 2nd edn (New Jersey: Wiley)
[2] Makabe T and Petrović Z 2006 *Plasma Electronics: Applications in Microelectronic Device Fabrication* (London: Taylor and Francis)

[3] Chabert P and Braithwaite N 2011 *Physics of Radio-Frequency Plasmas* (Cambridge: Cambridge University Press)
[4] Hamaoka F, Yagisawa T and Makabe T 2007 *IEEE Trans. Plasma Sci.* **35** 1350
[5] Oehrlein G S and Hamaguchi S 2018 *Plasma Sources Sci. Technol.* **27** 023001
[6] Lafleur T 2016 *Plasma Sources Sci. Technol.* **25** 013001
[7] Kitajima T, Takeo Y, Petrović Z L and Makabe T 2000 *Appl. Phys. Lett.* **77** 849
[8] Boyle P C, Ellingboe A R and Turner M M 2004 *Plasma Sourc. Sci. Technol.* **13** 493
[9] Boyle P C, Ellingboe A R and Turner M M 2004 *J. Phys. D: Appl. Phys.* **37** 697
[10] Georgieva V, Bogaerts A and Gijbels R 2004 *Phys. Rev.* E **69** 026406
[11] Lee J K, Manuilenko O V, Babaeva N Y, Kim H C and Shon J W 2005 *Plasma Sources Sci. Technol.* **14** 89
[12] Wang S, Xu X and Wang Y-N 2007 *Physi. Plasmas* **14** 113501
[13] Heil B G, Czarnetzki U, Brinkmann R P and Mussenbrock T 2008 *J. Phys. D: Appl. Phys.* **41** 165202
[14] Schulze J, Schüngel E, Donkó Z and Czarnetzki U 2010 *Plasma Sources Sci. Technol.* **19** 045028
[15] Schulze J, Schüngel E, Czarnetzki U, Gebhardt M, Brinkmann R P and Mussenbrock T 2011 *Appl. Phys. Lett.* **98** 031501
[16] Schüngel E, Schulze J, Donkó Z and Czarnetzki U 2011 *Phys. Plasmas* **18** 013503
[17] Schulze J, Schüngel E, Donkó Z and Czarnetzki U 2011 *Plasma Sources Sci. Technol.* **20** 015017
[18] Lafleur T, Boswell R W and Booth J P 2012 *Appl. Phys. Lett.* **100** 194101
[19] Johnson E V, Delattre P A and Booth J P 2012 *Appl. Phys. Lett.* **100** 133504
[20] Bienholz S, Styrnoll T and Awakowicz P 2014 *J. Phys. D: Appl. Phys.* **47** 065201
[21] Diomede P, Economou D J, Lafleur T, Booth J P and Longo S 2014 *Plasma Sources Sci. Technol.* **23** 065049
[22] Bruneau B, Gans T, O'Connell D, Greb A, Johnson E V and Booth J P 2015 *Phys. Rev. Lett.* **114** 125002
[23] Zhang Y, Zafar A, Coumou D J, Shannon S C and Kushner M J 2015 *J. Appl. Phys.* **117** 233302
[24] Birdsall C K and Langdon A B 1985 *Plasma Physics via Computer Simulation* (New York: McGraw-Hill)
[25] Hockney R W and Eastwood J W 1981 *Computer Simulation Using Particles* (New York: McGraw-Hill)
[26] Birdsall C K 1991 *IEEE Trans. Plasma Sci.* **19** 65
[27] Diomede P, Capitelli M and Longo S 2005 *Plasma Sources Sci. Technol.* **14** 459
[28] Matyash K, Schneider R, Taccogna F, Hatazarna A, Longo S, Capitelli M, Tskhakaya D and Bronold F X 2007 *Contrib. Plasma Phys.* **47** 595
[29] Donkó Z 2011 *Plasma Sources Sci. Technol.* **20** 024001
[30] Donkó Z, Schulze J, Czarnetzki U, Derzsi A, Hartmann P, Korolov I and Schüngel E 2012 *Plasma Phys. Control. Fusion* **54** 124003
[31] Sun A, Becker M and Loffhagen D 2016 *Comput. Phys. Commun.* **206** 35
[32] Surendra M and Graves D B 1991 *IEEE Trans. Plasma Sci.* **19** 144
[33] Verboncoeur J P 2005 *Plasma Phys. Control. Fusion* **47** A231
[34] Kushner M J 1983 *J. Appl. Phys.* **54** 4958
[35] Tavant A, Lucken R, Bourdon A and Chabert P 2019 *Plasma Sources Sci. Technol.* **28** 075007
[36] Derzsi A, Korolov I, Schüngel E, Donkó Z and Schulze J 2015 *Plasma Sources Sci. Technol.* **24** 034002
[37] Korolov I, Derzsi A, Donkó Z, Schüngel E and Schulze J 2016 *Plasma Sources Sci. Technol.* **25** 015024
[38] Braginsky O, Kovalev A, Lopaev D, Proshina O, Rakhimova T, Vasilieva A, Voloshin D and Zyryanov S 2012 *J. Phys. D.* **45** 015201
[39] Bojarov A, Radmilović-Radjenović M and Petrović Z L 2010 *Proc. 20th ESCAMPIG* Novi Sad, Serbia 13-17 July 2010
Bojarov A, Radmilović-Radjenović M and Petrović Z L 2010 *Publ. Astron. Obs. Belgrade* **89** 131
Bojarov A, Radmilović-Radjenović M and Petrović Z L 2012 *Proc. 65th Annual Gaseous Electronics Conf.* Austin, Texas 22-26 October 2012
Bojarov A, Radmilović-Radjenović M and Petrović Z L 2014 *Proc. 27th Summer School and International Symposium on the Physics of Ionized Gases* (Belgrade, Serbia 26-29 August 2014)
[40] Radmilović-Radjenović M and Petrović Z L 2009 *Eur. Phys. J.* D **54** 445
[41] Gudmundsson J T, Kawamura E and Lieberman M A 2013 *Plasma Sources Sci. Technol.* **22** 035011
[42] Hannesdottir H and Gudmundsson J T 2016 *Plasma Sources Sci. Technol.* **25** 055002
[43] Greb A, Niemi K, O'Connell D and Gans T 2013 *Appl. Phys. Lett.* **103** 244101
[44] Horváth B, Daksha M, Korolov I, Derzsi A and Schulze J 2017 *Plasma Sourc. Sci. Technol.* **26** 124001
[45] Horváth B, Schulze J, Donkó Z and Derzsi A 2018 *J. Phys. D: Appl. Phys.* **51** 355204
[46] Sun A, Becker M and Loffhagen D 2018 *Plasma Sources Sci. Technol.* **27** 054002
[47] Daksha M, Berger B, Schüngel E, Korolov I, Derzsi A, Koepke M, Donkó Z and Schulze J 2016 *J. Phys. D: Appl. Phys* **49** 234001
[48] Daksha M, Derzsi A, Donkó Z and Schulze J 2019 *Plasma Sources Sci. Technol.* **28** 034002
[49] Derzsi A, Horváth B, Korolov I, Donkó Z and Schulze J 2019 *J. Appl. Phys.* **126** 043303
[50] Belenguer P and Boeuf J P 1990 *Phys. Rev.* A **41** 4447
[51] Schulze J, Heil B G, Luggenhölscher D and Czarnetzki U 2008 *IEEE Trans. Plasma Sci.* **36** 1400
[52] Schulze J, Heil B G, Luggenhölscher D, Brinkmann R P and Czarnetzki U 2008 *J. Phys.* D **41** 195212
[53] Schulze J, Kampschulte T, Luggenhölscher D, Brinkmann R P and Czarnetzki U 2008 *J. Phys. Conf. Ser.* **86** 12010
[54] Turner M M 2009 *J. Phys.* D **42** 194008
[55] Mussenbrock T, Brinkmann R P, Lieberman M A, Lichtenberg A J and Kawamura E 2008 *Phys. Rev. Lett.* **101** 085004
[56] Schweigert V A, Alexandrov A L, Gimelshtein S F and Ivanov M S 1999 *Plasma Sources Sci. Technol.* **8** B1
[57] Ivanov V V, Popov A M and Rakhimova T V 1995 *Plasma Phys. Rep.* **21** 515
[58] Dittmann K, Drozdov D, Krames B and Meichsner J 2007 *J. Phys. D: Appl. Phys.* **40** 6593
[59] Donkó Z, Schulze J, Hartmann P, Korolov I, Czarnetzki U and Schüngel E 2010 *Appl. Phys. Lett.* **97** 081501
[60] Schulze J, Donkó Z, Schüngel E and Czarnetzki U 2011 *Plasma Sources Sci. Technol.* **20** 045007
[61] Turner M M, Chabert P, Levif P, Boyle P and Robiche J 2007 *Proc. 18th ICPIG* Prague, Czech Republic
[62] Booth J P, Curley G, Marić D and Chabert P 2010 *Plasma Sources Sci. Technol.* **19** 015005
[63] Böhm C and Perrin J 1993 *Rev. Sci. Instrum.* **64** 31
[64] Liu Q, Liu Y, Samir T and Ma Z 2014 *Phys. Plasmas* **21** 083511
[65] Lafleur T, Chabert P and Booth J P 2013 *J. Phys. D: Appl. Phys.* **46** 135201
[66] Korolov I, Derzsi A, Donkó Z and Schulze J 2013 *Appl. Phys. Lett.* **103** 064102
[67] Czarnetzki U, Heil B G, Schulze J, Donkó Z, Mussenbrock T and Brinkmann R P 2009 *J. Phys. Conf. Ser.* **162** 012010
[68] Daksha M, Derzsi A, Wilczek S, Trieschmann J, Mussenbrock T, Awakowicz P, Donkó Z and Schulze J 2017 *Plasma Sources Sci. Technol.* **26** 085006

[69] Bronold F X, Matyash K, Tskhakaya D, Schneider R and Fehske H 2007 *J. Phys. D: Appl. Phys.* **40** 6583
[70] Kullig C, Dittmann K, Wegner T, Sheykin I, Matyash K, Loffhagen D, Schneider R and Meichsner J 2012 *Contrib. Plasma Phys.* **52** 836
[71] Wenn Y-Y, Zhang Y-R, Jiang G, Song Y-H and Wang Y-N 2019 *AIP Adv.* **9** 055019
[72] Wang L, Wen D-Q, Zhang Q-Z, Song Y-H, Zhang Y-R and Wang Y-N 2019 *Plasma Sources Sci. Technol.* **28** 055007
[73] Phelps A V and Petrović Z L 1999 *Plasma Sources Sci. Technol.* **8** R21
[74] Donkó Z 2000 *J. Appl. Phys* **88** 2226
[75] Donkó Z 2001 *Phys. Rev.* E **64** 026401
[76] Kollath R 1956 *Encyclopedia of Physics* ed S Flügge (Berlin: Springer) vol 21 p 264
[77] Sun J-Y, Wen D-Q, Zhang Q-Z, Liu Y-X and Wang Y-N 2019 *Phys. Plasmas* **26** 063505
[78] Sun J-Y, Zhang Q-Z, Liu Y-X and Wang Y-N 2019 *Plasma Sources Sci. Technol.* accepted https://doi.org/10.1088/1361-6595/ab6c80
[79] Matsunami N *et al* 1984 *Atomic Data Nucl. Data Tables* **31** 1
[80] Trieschmann J and Mussenbrock T 2015 *J. Appl. Phys.* **118** 033302
[81] Trieschmann J, Schmidt F and Mussenbrock T 2016 *Plasma Process Polym.* **4** 1600140
[82] Krüger F, Gergs T and Trieschmann J 2019 *Plasma Sources Sci. Technol.* **28** 035002
[83] Bogaerts A and Gijbels R 1996 *J. Appl. Phys.* **79** 1279
[84] Bogaerts A and Gijbels R 1996 *Anal. Chem.* **68** 2676
[85] Bogaerts A, Gijbels R and Carman R J 1998 *Spectrochim. Acta Part* B **53** 1679
[86] Bogaerts A, Okhrimovskyy A, Baguer N and Gijbels R 2005 *Plasma Sources Sci. Technol.* **14** 191
[87] Kolev I and Bogaerts A 2006 *Plasma Plasma Process Polym* **3** 127
[88] Bogaerts A, Bultinck E, Kolev I, Schwaederle L, von Aeken K, Buyle G and Depla D 2009 *J. Phys. D: Appl. Phys.* **42** 194018
[89] Hecimovic A, Maszl C, Schulz-von der Gathen V, Boke M and von Keudell A 2016 *Plasma Sources Sci. Technol.* **25** 035001
[90] Hecimovic A, Corbella C, Maszl C, Breilmann W and von Keudell A 2017 *J. Appl. Phys.* **121** 171915
[91] Kozak T and Lazar J 2019 *Plasma Sources Sci. Technol.* **27** 115012
[92] Held J and von Keudell A 2019 *Plasma Chem Plasma Process* **40** 643
[93] Ries S, Banko L, Hans M, Primetzhofer D, Schneider J M, Ludwig A, Awakowicz P and Schulze J 2019 *Plasma Sources Sci. Technol.* **28** 114001
[94] Brenning N, Gudmundsson J T, Raadu M A, Petty T J, Minea T and Lundin D 2017 *Plasma Sources Sci. Technol.* **26** 125003
[95] Held J, Hecimovic A, von Keudell A and Schulz-von der Gathen V 2018 *Plasma Sources Sci. Technol.* **27** 105012
[96] Anders A 2011 *Surf. Coat. Technol.* **205** S1
[97] Phelps A V www.colorado.edu/ ∼avp/collision_data/ unpublished
[98] Phelps A V 1991 *J. Phys. Chem. Ref. Data* **20** 557
[99] Phelps A V 1994 *J. Appl. Phys.* **76** 747
[100] Vriens L 1964 *Phys. Lett.* **8** 260
[101] Lindhard J, Scharff M and Schiott H E 1963 *Mat. Fys. Medd. Dan. Vid. Selsk* **33** 14
[102] Coburn J W and Kay E 1971 *Appl. Phys. Lett.* **18** 435
[103] Sydorenko D, Smolyakovl A, Kaganovich I D and Raitses Y 2006 *Phys. Plasmas* **13** 014501
[104] Vaughan J R M 1989 *IEEE Trans. Electron Devices* **36** 1963
[105] Vaughan J R M 1993 *IEEE Trans. Electron Devices* **40** 830
[106] Seiler H 1983 *J. Appl. Phys.* **54** R1–R18
[107] Ruzic D, Moore R, Manos D and Cohen S 1981 *J. Vac. Sci. Technol.* **20** 1313
[108] Walker C G H, El-Gomati M M, Assa'd A M D and Zadraz'il M 2008 *Scanning* **30** 365
[109] Gonzales L A, Angelucci M, Larciprete R and Cimino R 2017 *AIP Adv.* **7** 115203
[110] Raitses Y, Kaganovich I, Khrabrov A, Sydorenko D, Fisch N J and Smolyakov A 2011 *IEEE Trans. Plasma Sci.* **39** 995
[111] Gopinath V P, Verboncoeur J P and Birdsall C K 1998 *Phys. Plasmas* **5** 1535
[112] Barral S, Makowski K and Peradzynsky Z 2003 *Phys. Plasmas* **10** 4137
[113] Bronshtein I M and Fraiman B S 1969 *Secondary Electron Emission* (Moscow: Atomizdat)
[114] Sigmund P 1969 *Phys. Rev.* **184** 383
[115] Greenwood J 2002 *Vacuum* **67** 217
[116] Mussenbrock T and Brinkmann R P 2006 *Appl. Phys. Lett.* **88** 151503
[117] Czarnetzki U, Mussenbrock T and Brinkmann R P 2006 *Phys. Plasmas* **13** 123503
[118] Mussenbrock T and Brinkmann R P 2007 *Plasma Sources Sci. Technol.* **16** 377
[119] Donkó Z, Schulze J, Czarnetzki U and Luggenhölscher D 2009 *Appl. Phys. Lett.* **94** 131501
[120] Krüger F, Wilczek S, Mussenbrock T and Schulze J 2019 *Plasma Sources Sci. Technol.* **28** 075017
[121] Wilczek S, Trieschmann J, Schulze J, Schuengel E, Brinkmann R P, Derzsi A, Korolov I, Donkó Z and Mussenbrock T 2015 *Plasma Sources Sci. Technol.* **24** 024002
[122] Wilczek S *et al* 2016 *Phys. Plasmas* **23** 063514
[123] Wilczek S, Trieschmann J, Schulze J, Donkó Z, Brinkmann R P and Mussenbrock T 2018 *Plasma Sources Sci. Technol.* **27** 125010
[124] Berger B, You K, Lee H-C, Mussenbrock T, Awakowicz P and Schulze J 2018 *Plasma Sources Sci. Technol.* **27** 12LT02